N72-20819

Final Report
Contract NAS 8-21315

"Application of Numerical Methods to Extend Capabilities for Optimal Rocket Guidance"

Report on Reentry Guidance of Shuttle Orbiter
and
Summary of All Work on Contract NAS 8-21315

Submitted March 8, 1972, to

National Aeronautics and Space Administration
George C. Marshall Space Flight Center
Marshall Space Flight Center
Huntsville, Alabama 35812

Submitted by

IBM Federal Systems Division
18100 Frederick Pike
Gaithersburg, Maryland 20760

Work performed at

Advanced Systems Development Department
24 New England Executive Park
Burlington, Mass. 01803

Contents

1. Introduction

This Report describes that portion of work done under contract NAS 8-21315 which concerns the reentry guidance of the shuttle orbiter.

1.1 Reentry Requirements

At the start of reentry, the shuttle orbiter may be assumed to be in a circular orbit at approximately 100 n.mi. altitude. From this condition, it is to be brought near a landing site. At the end of its glide toward the site, the craft should reach an altitude, airspeed, and flight path angle at which the air-breathing engines can be turned on, and the craft flown manually to a landing.

A typical reentry begins with a retrofire of the rocket engines such that the flight path is one or two degrees below horizontal at the time aerodynamic force reaches .01 of gravity. As the vehicle plunges deeper into the atmosphere, the trajectory must be controlled to prevent excessive deceleration or skin temperature. In addition, the entire history of heat flow through the skin and insulation must be controlled to prevent excessive cabin temperature.

1.2 Footprint as a Measure of Performance

Before retrofire, the set of possible landing points for some fixed future time interval is a band centered on the subsatellite trace. After retrofire, the set of reachable points is much reduced, and continues to shrink as reentry progresses. Since atmospheric density and winds, vehicle aerodynamics, efficacy of control actions, etc., are known only approximately, it is prudent to reenter so that at all times the desired terminal state remains well inside what the reentry planner estimates to be the boundary of the reachable set.

It follows that a desirable feature of a guidance algorithm is that, in addition to meeting constraints on deceleration and heating, it should produce a large reachable set. In the work to be reported here, we consider a subset of the reachable set which we define to be the positions attainable at a specified terminal altitude. We refer to this set of reachable positions as a "footprint" and use it as a measure of performance for guidance schemes. The airspeed and path angle associated with trajectories which reach the boundary of the footprint appear to be suitable initial conditions for maneuvers leading to powered flight.

1.3 Role of Optimal Trajectories

Trajectories which reach the boundary of our reachable set are necessarily optimal with respect to the performance index

$$J = s^T x(t_f) \tag{1.3-1}$$

for some s. Each boundary point is the terminus of the unique trajectory which maximizes J subject to the constraint $h_f = h_d$, where s is a unit n-vector, t_f is final time, x_f is final state, h_f is final altitude, and h_d is desired final altitude. For each value of s, the optimal trajectory reaches the boundary of the reachable set at the point $x(t_f)$ at which the locus $s^T x = s^T x(t_f)$ is tangent to the reachable set. By maximizing J for an appropriate sequence of values of s, we generate a reentry footprint.

The trajectories forming our footprint have constant 30° angle of attack and variable bank angle. Although deceleration and heating are unconstrained, no trajectory has aerodynamic deceleration above 1.25g or skin temperature above 2400°F, and these peak values can be reduced by increasing initial path angle.

In addition to serving as a standard for measuring performance loss due to suboptimal guidance, the optimal trajectories suggest functional forms for parameterized guidance laws. One may parameterize a control history to imitate the optimal control history, or parameterize costate to imitate optimal costate, then iterate on the parameters to meet end conditions.

The trajectories also show that optimal state, costate and control histories consist of smooth functions with a superimposed oscillation. This information may be useful in designing numerical integration methods which partition solutions into slowly-varying and oscillatory parts. It also suggests the use of guidance which damps the oscillation.

1.4 Outline of Report

Section 2 and Appendix A1 present the coordinate systems, aerodynamics, equations of motion, and numerical constants used in the Report. Section 3 and Appendices A2 and A3 describe the computation of the footprint. Section 4 presents numerical results for a suboptimal scheme which generates reentry trajectories subject to constraints on heating rate and aerodynamic acceleration. Section 5 summarizes our work on contract NAS 8-21315 since its inception.

2. Reentry Dynamics and Aerodynamics

For the purpose of reentry guidance, we regard the attitude of the vehicle as being instantaneously controllable , we consider only translational dynamics as affected by lift, drag and gravitational forces, disregarding forces which may be required for attitude control. For the purposes of obtaining the data presented in this report and to facilitate geometrical insights, we have used equations of motion in spherical coordinates. Although it is possible to include the effect of rotation of the earth's atmosphere in these equations, we have not done so because we felt the additional complexity thus introduced would be an unnecessary burden at this point in our investigations. Thus, we regard the earth as being an inertially-fixed, homogeneous sphere with an exponential atmosphere.

The simplified force model we use is shown in figure 2-1 where $\bar{r}$ is a vector defining the position of the vehicle center of mass in an inertially-fixed, earth-centered cartesian coordinate (ECCC) system. The vector $\bar{v}$ is the time derivative of $\bar{r}$ and $\bar{g}$ is gravitational acceleration given by

$$\bar{g} = -\frac{\mu}{r^3}\bar{r} \qquad (2\text{-}1)$$

where $r = |\bar{r}|$.

The vector $\bar{L}$ represents aerodynamic lift force which is normal to $\bar{v}$ and $\bar{D}$ represents aerodynamic drag force which is antiparallel to $\bar{v}$. The magnitude of the lift and drag forces may be expressed as

$$\begin{aligned} L &= \frac{1}{2}\rho\, v^2\, S\, C_L(\alpha) \\ D &= \frac{1}{2}\rho\, v^2\, S\, C_D(\alpha) \end{aligned} \qquad (2\ 2)$$

where S is the planform area of the vehicle, C_L is the coefficient of lift, C_D is the coefficient of drag and ρ is atmospheric density. The coefficients of lift and drag depend on mach number as well as angle of attack but the dependence is not too strong at hypersonic velocities and since we shall be

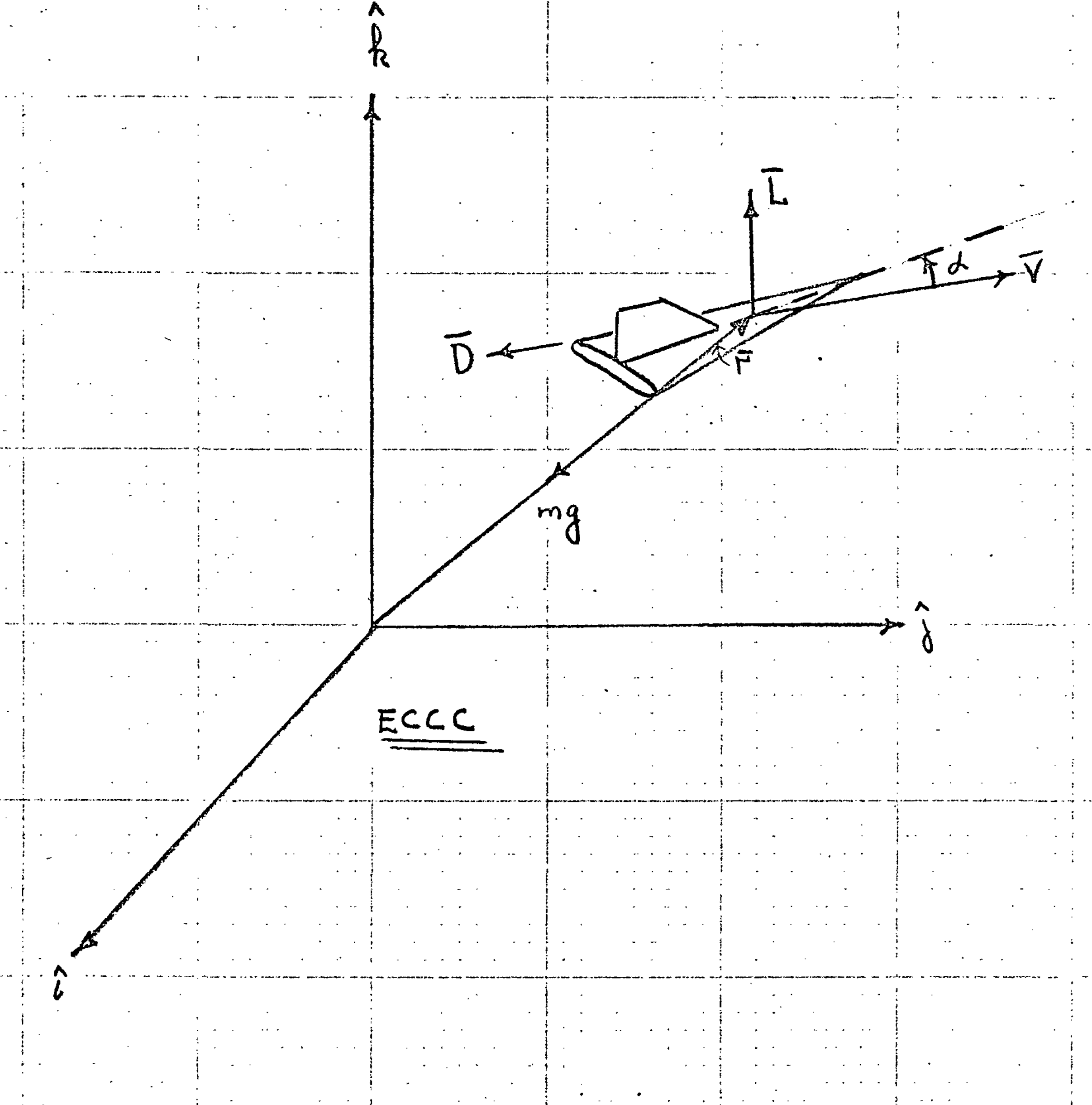

FIGURE 2-1 SIMPLIFIED FORCE MODEL

interested mainly in this flight regime, we neglect it. We use a four-parameter model for hypersonic C_L and C_D as functions of angle of attack and atmospheric density is computed as an exponential function of altitude. These models are discussed in appendix A1.

Relative to the ECCC system of figure 2-1, the equations of motion of the vehicle are

$$\dot{\bar{r}} = \bar{v}$$

$$\dot{\bar{v}} = \bar{g} + \frac{\bar{L}}{m} + \frac{\bar{D}}{m} \qquad (2\text{-}3)$$

where m is the vehicle mass. We should like to express these equations in spherical coordinates. To this end, we define spherical coordinates of position relative to the ECCC system as shown in figure 2-2. Several interpretations of the angular coordinates of position, ϕ and λ, are possible depending on the orientation of the ECCC system and the initial conditions subject to which the equations of motion are solved. For example, let $\hat{i}$ and $\hat{j}$ span the earth's equatorial plane, let $\hat{k}$ point in a northerly direction, and let ϕ and λ be initialized, respectively, with the longitude and latitude of vehicle position at the initial time. If latitude is measured positively north of the equator and longitude positively east of the prime meridian, then λ and ϕ at any time are equal to true latitude and true longitude, respectively. As a further example, if $\hat{i}$ points toward the position of the vehicle at the initial time and if $\hat{j}$ lies in the initial $(\bar{r},\bar{v})$ plane, then ϕ is down-range angle and λ is cross-range angle.

We now define spherical coordinates of velocity relative to the $(\hat{r}, \hat{\phi}, \hat{\lambda})$ position-oriented cartesian coordinate (RCC) system as shown in figure 2-3 where the unit vector $\hat{r}$ points in the direction of increasing r, $\hat{\phi}$ in the direction of increasing ϕ, and $\hat{\lambda}$ in the direction of increasing λ. Several interpretations of the angular coordinate ψ are possible depending on the orientation of the ECCC system. For example, if $\hat{i}$ and $\hat{j}$ are chosen to span the equatorial plane, and if $\lambda < \frac{\pi}{2}$, then $\hat{\phi}$ points in a locally

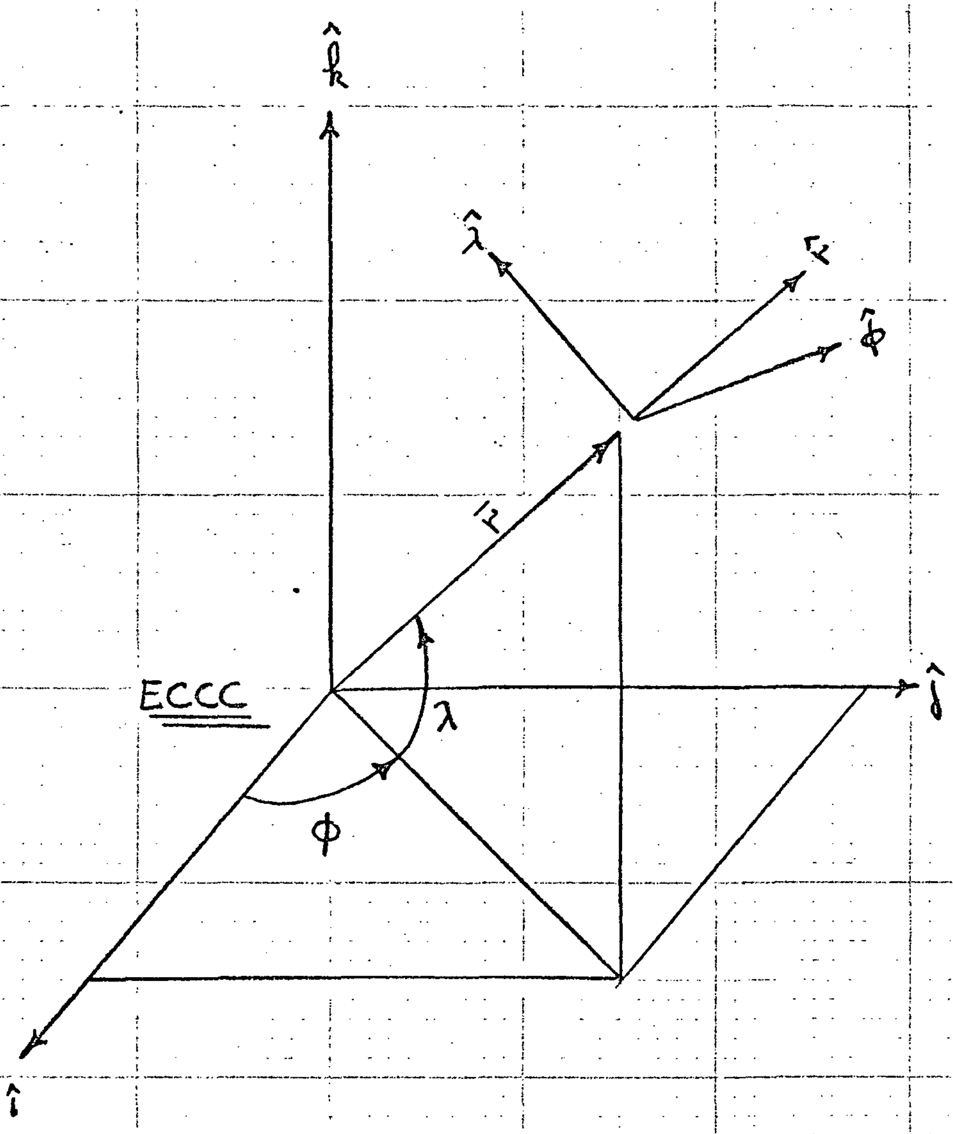

FIGURE 2-2 SPHERICAL COORDINATES OF POSITION RELATIVE ECCC SYSTEM

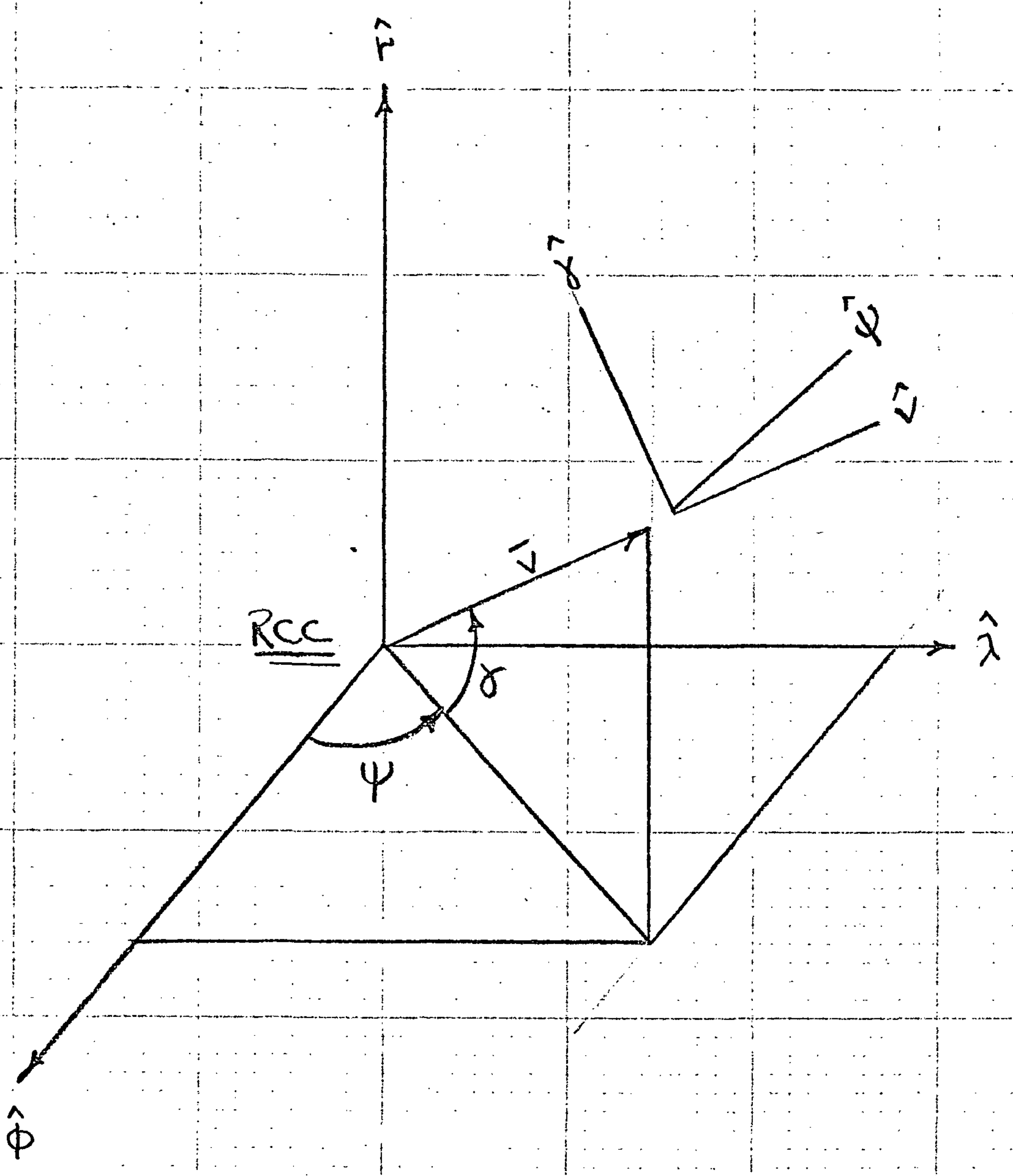

FIGURE 2-3 SPHERICAL COORDINATES OF VELOCITY RELATIVE TO RCC SYSTEM

easterly direction and $\hat{\lambda}$ in a locally northerly direction and ψ is heading angle measured positively north from an easterly direction. On the other hand, if $\hat{i}$ points toward the position of the vehicle at the initial time and if $\hat{j}$ lies in the initial $(\bar{r},\bar{v})$ plane, then $\hat{\phi}$ points downrange, $\hat{\lambda}$ points crossrange and ψ is heading angle relative to the downrange direction measured by a positive rotation about $\hat{r}$. In either case, the $(\hat{\phi},\hat{\lambda})$ plane is locally horizontal so that γ is the inclination of the velocity vector above the local horizontal.

The lift and drag forces are defined relative to the $(\hat{v},\hat{\psi},\hat{\gamma})$ velocity-oriented cartesian coordinate (VCC) system of figure 2-4. Here the drag vector is antiparallel to $\hat{v}$ and the lift vector lies in the $(\hat{\psi},\hat{\gamma})$ plane making an angle of β with $\hat{j}$.

The equations of motion relative to these spherical coordinates are derived in reference 1 as

$$\begin{aligned}
\dot{r} &= v \sin\gamma \\
\dot{\phi} &= \frac{v \cos\gamma \cos\psi}{r \cos\lambda} \\
\dot{\lambda} &= \frac{v \cos\gamma \sin\psi}{r} \\
\dot{v} &= -\frac{D}{m} - \frac{\mu}{r^2} \sin\gamma \\
\dot{\gamma} &= \frac{L \cos\beta}{mv} - \frac{\mu}{r^2 v} \cos\gamma + \frac{v}{r} \cos\gamma \\
\dot{\psi} &= \frac{L \sin\beta}{mv \cos\gamma} - \frac{v \cos\gamma \cos\psi}{r \cot\lambda}
\end{aligned} \tag{2-4}$$

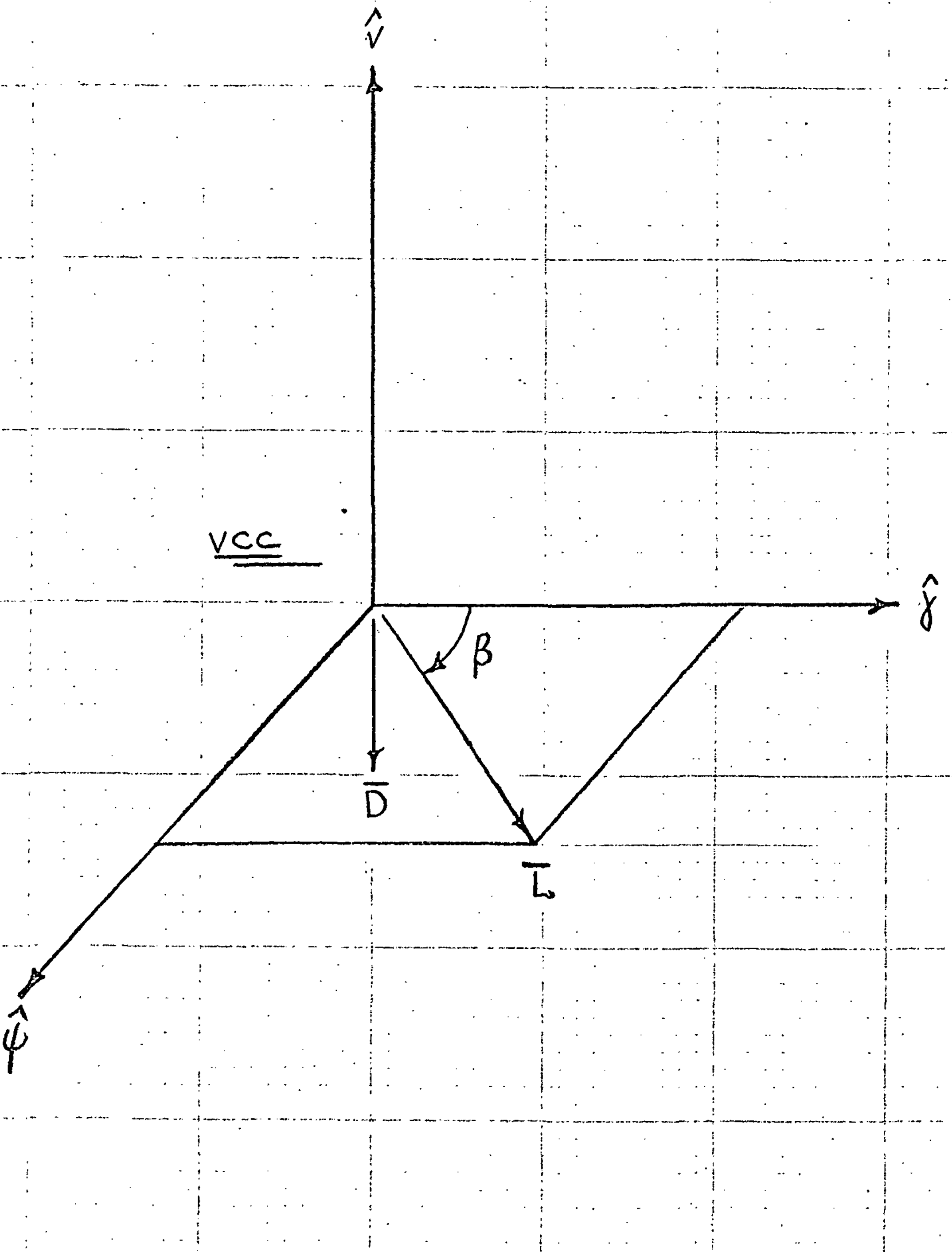

FIGURE 2-4 SPHERICAL COORDINATES OF CONTROL RELATIVE TO VCC SYSTEM

3. Unconstrained Reentry Footprint

3.1 Introduction

The importance of a reentry footprint during inflight targeting and guidance is obvious -- for safety and stability, a vehicle's control system must try to achieve a destination within its reachable set. Moreover, a reentry footprint can be an important factor during both vehicle design and guidance algorithm development. In addition to indicating the stability and ease of convergence of a reentry formulation, calculating reentry footprints gives insight into the behavior of state and control variables during optimal trajectories. Such insight can be vital to understanding the tradeoffs involved between constraining heating and aerodynamic forces, and maximizing cross range capability, guidance stability, and computational speed and can lead to safe, effective targeting and guidance schemes.

In the following paragraphs, we present an unconstrained reentry footprint for a shuttle vehicle which enters the earth's atmosphere at 93 km. initial altitude after deboost from a near earth orbit. The reentry trajectories used to generate the footprint have bank angle β as control. The angle of attack is held constant at the maximum lift/drag ratio consistent with vehicle design, and earth rotation is ignored. After briefly describing the method of computation, we present graphs illustrating the footprint and the variation of state and control variables along it. We discuss the effects of constraints and of variations in initial state upon the footprint.

3.2 Method of Computation

We calculated the unconstrained footprint presented in the following section by maximizing the cost functional

$$J = \Theta\lambda_f + (1-\Theta)\phi_f \qquad (3\text{-}1)$$

for values of Θ ranging from 0.0 (maximum downrange case) to 1.0 (maximum crossrange case). Here, λ_f and ϕ_f are the final crossrange and downrange, respectively. We used the six differential equations for state components ρ, v, γ, ψ, ϕ, and λ presented in Section 2 in a Mayer formulation with Hamiltonian $H = p^T\dot{x}$. As shown in Appendix A2, the problem was reduced to choosing initial values for p_ρ, p_γ, p_ψ, and p_λ (components of costate adjoint to ρ, γ, ψ, and λ, respectively) so that the end conditions at final time t_f

$$\begin{aligned} p_\gamma(t_f) &= 0 \\ p_\psi(t_f) &= 0 \\ p_\lambda(t_f) &= \Theta \\ p_v(t_f) &= 0 \end{aligned} \tag{3-2}$$

were satisfied. Values of state and costate at t_f were obtained by integrating the state equations (2-4) and (A2-1)* and costate equations (A2-5) until the desired final altitude was obtained. The control β (bank angle) was selected from equations (A2-4) using values of p_γ, p_ψ and $\cos\gamma$. As described in Appendix A3, a quadratic extrapolation technique was used to initialize p_ρ, p_γ, p_ψ, and p_λ accurately enough for a finite-difference Newton-Raphson procedure to converge each optimal trajectory along the footprint.

3.3 Shape of Footprint

Figure 3-1 illustrates the smooth, convex shape of the reentry footprint from the maximum cross range point ($\Theta = 1.0$) to the maximum downrange point ($\Theta = 0.0$). Over 1350 nautical miles cross range are achieved.

---

*The state differential equation for ρ is given in Appendix A2.

The dashed lines illustrate paths of reentry trajectories to three points on the footprint. Points 4 to 6 show values of ϕ_f and λ_f for three feasible trajectories generated using the algorithm described in Section 4 of this report. Table 3-1 summarizes data for these six points, while Table A1-1 in Appendix A1 summarizes vehicle and initial state data for the trajectories.

Table 3-1 Explanation of Points on Fig. 3-1

Point	ϕ_f	λ_f	Method of Calculation
1	66.6	22.7	Optimal cross range trajectory
2	102.6	20.9	Optimal trajectory for $\Theta = 0.91$
3	144.5	0.0	Optimal down range trajectory
4	31.1	13.9	Feasible trajectory with $10.2 \text{x} 10^{18} = \rho v^6$ and 3g arcs
5	67.0	21.1	Feasible trajectory with $3.8 \times 10^{18} = \rho v^6$ and 1.5g arcs
6	70.2	20.8	Feasible trajectory with $5.6 \times 10^{18} = \rho v^6$ and 1.25g arcs

As shown in Figure 3-2, initial values of p_ρ, p_γ, and p_v are surprisingly linear functions of Θ,* while initial values of p_ψ and p_λ are slowly varying functions of Θ. Figure 3-3 illustrates the deviation of initial costate from linearity along the footprint arc $\theta=$ 0.9 to 1.0 . As shown by Figure 3-4, initial bank angle does not reach 90° along the front of the footprint ($|\Theta| \leq 1.0$).

3.4 Variation of State and Costate Along Trajectories

Figures 3-5 to 3-13 show details of the trajectories leading to

---

*The footprint parameter Θ is related to the angle x between the crossrange axis and the tangent to the footprint by $x = \arctan [\Theta/(1-\Theta]$.

points 1, 2, and 3 on the footprint on Figure 3-1. Although all three trajectories involve an oscillatory descent, aerodynamic accelerations never exceed 1.25 g's. Flight time for the trajectories increases with final downrange ϕ_f and velocity magnitude is a monotonic function of time after the first 100 sec. of each trajectory. None of the costate variables changes sign during optimal trajectories, although we often saw p_γ go negative when an initialization was outside the algorithm's region of convergence. Figure 3-12 illustrates such a case. Initial costate for ~p_γ in Figure 3-12 differs from the optimal initial costate by less than 0.3%. The behavior of state and costate variables during the last few hundred seconds of the trajectory for $\Theta = 1.0$ is similar to their behavior for $\Theta = 0.91$.

3.5 Effect of Initial State upon Results

Since costate $p = (\partial J/\partial x)$, initial values of p for optimal trajectories indicate the effect of variations in initial state upon final cross range and downrange. Table 3-2 lists values of initial costate for the optimal trajectories denoted by points 1, 2, and 3 in Figure 3-1.

Table 3-2

Θ	1.0	0.91	0.0
p_ρ	-839.319	-4490.23	-48,982.3
p_γ	0.315950	2.39840	28.6895
p_ψ	0.917802	0.895611	0.0
p_λ	0.397039	-0.164809	0.0
p_ϕ	0.0	0.09	1.0
p_v	$0.183885 \cdot 10^{-3}$	$0.455339 \cdot 10^{-3}$	$4.98680 \cdot 10^{-3}$

As seen from the Table, increasing initial v increases ϕ_f and λ_f while increasing initial ρ (decreasing initial altitude) decreases range. Since $p_\gamma(t_o) \sim 1/3$ for $\Theta = 1.0$, probably less than 1° more cross range would be gained by optimizing λ_f with respect to γ_o. (For the optimal γ_o, $p_\gamma(t_o) = 0.0$ and initial $\beta = 90°$ if $p_\psi > 0.$). Figure 3-15 illustrates the change in the optimal crossrange trajectory caused by increasing $\gamma(t_o)$ by 0.275°. The trajectory seems to become smoother as the optimum value of γ_o is approached, although we only obtained 0.08° more cross range from this increase in γ_o.

3.6 Heating and G-limit Constraints

Figures 3-15, 3-16, 3-17, and 3-18 show radiation equilibrium temperatures during the various optimal trajectories described above. None of the trajectories would violate a heating constraint of 2400°F, but the maximum crossrange trajectory for $\gamma(t_o) = -1.14$ exceeds 2300°F. However, a comparison of Figures 3-15 and 3-16 indicates that peak heating can be significantly reduced by varying initial path angle. Aerodynamic acceleration for the trajectories were shown in Figures 3-5, 3-8, and 3-11. For heating limit constraints above 2400°F and reasonable G-limit constraints, our unconstrained reentry footprint does not violate either heating or G-limit constraints and would thus be the same as a constrained one.

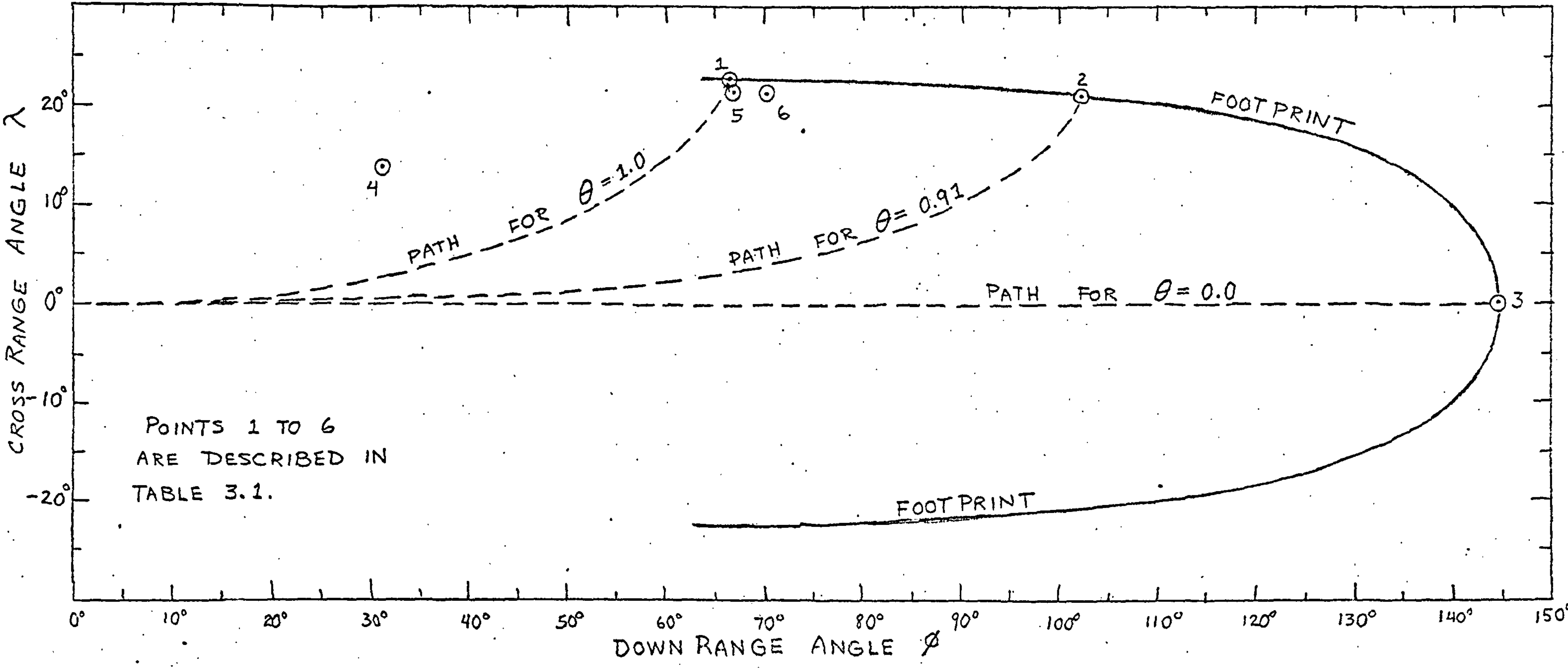

POINTS 1 TO 6
ARE DESCRIBED IN
TABLE 3.1.

FIGURE 3-1 REENTRY FOOTPRINT

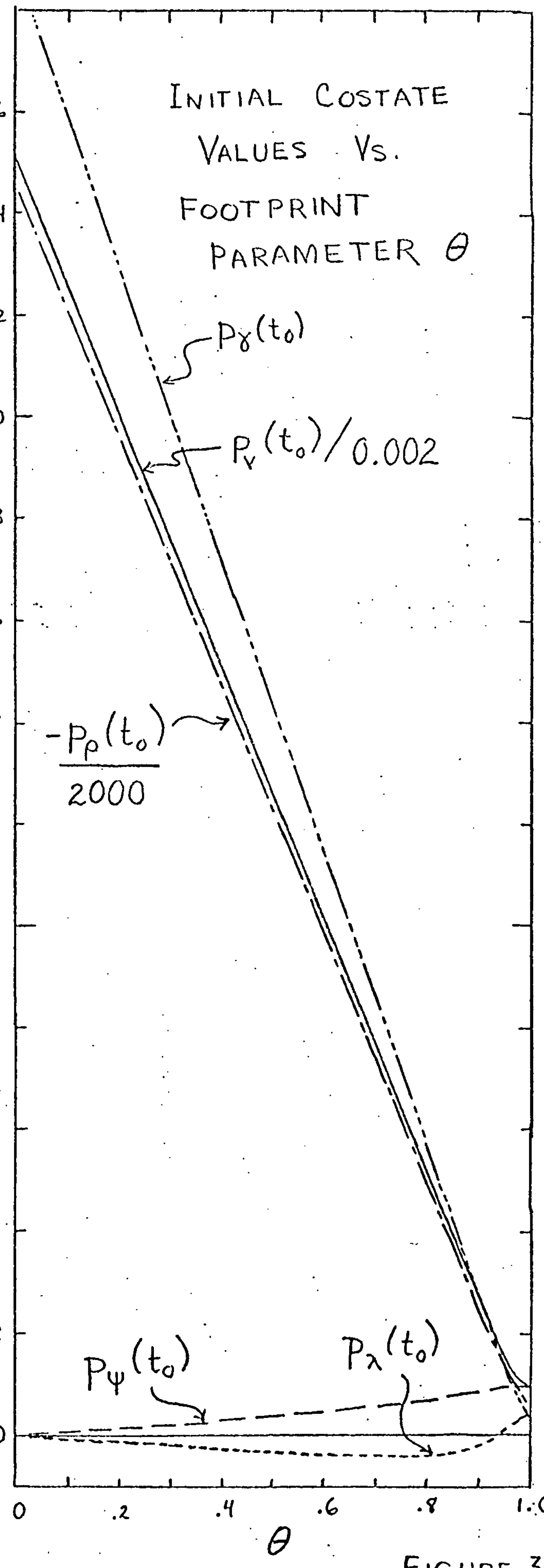
INITIAL COSTATE VALUES VS. FOOTPRINT PARAMETER θ
$P_\gamma(t_0)$
$P_v(t_0)/0.002$
$-P_\rho(t_0)/2000$
$P_\psi(t_0)$
$P_\lambda(t_0)$
26
24
22
20
18
16
14
12
10
8
6
4
2
0
0
.2
.4
.6
.8
1.0
θ

FIGURE 3-2

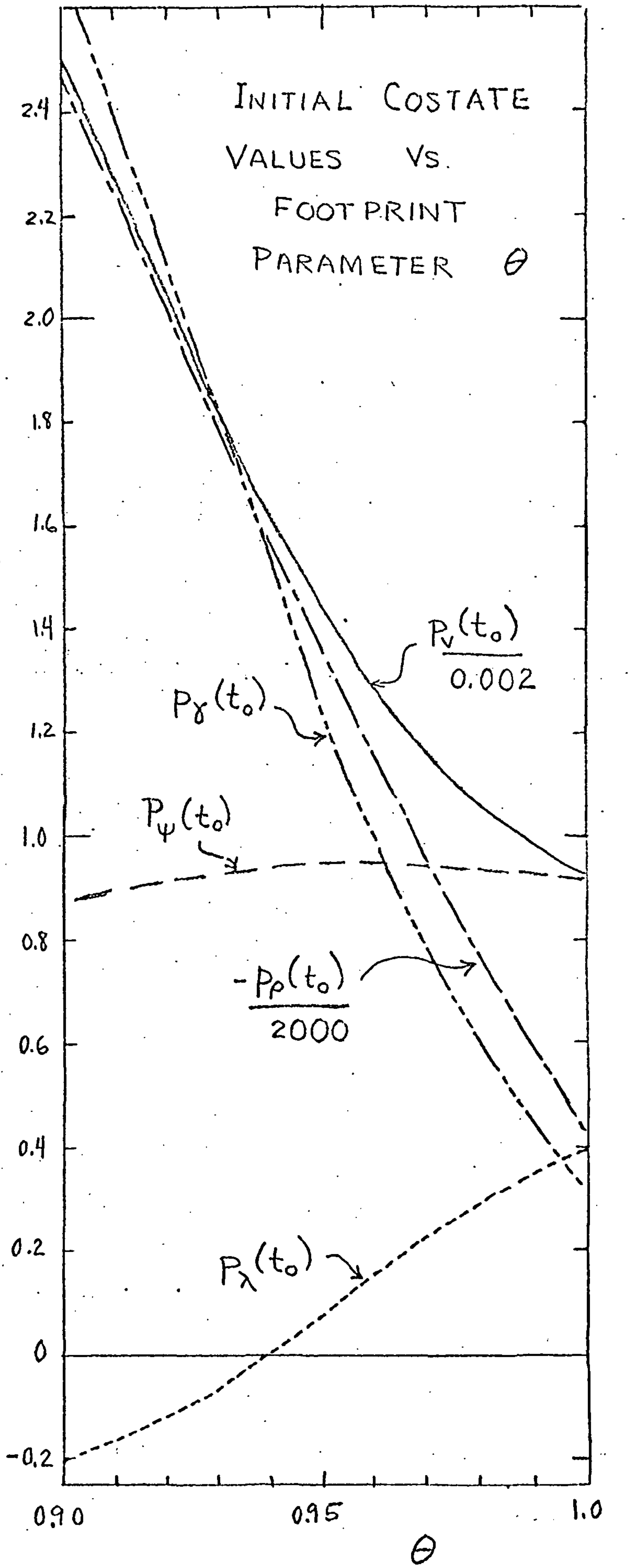
INITIAL COSTATE VALUES VS. FOOTPRINT PARAMETER θ
2.4
2.2
2.0
1.8
1.6
1.4
1.2
1.0
0.8
0.6
0.4
0.2
0
-0.2
0.90
0.95
1.0
θ
$\frac{P_v(t_o)}{0.002}$
$P_\gamma(t_o)$
$P_\psi(t_o)$
$\frac{-P_\rho(t_o)}{2000}$
$P_\lambda(t_o)$

FIGURE 3-3

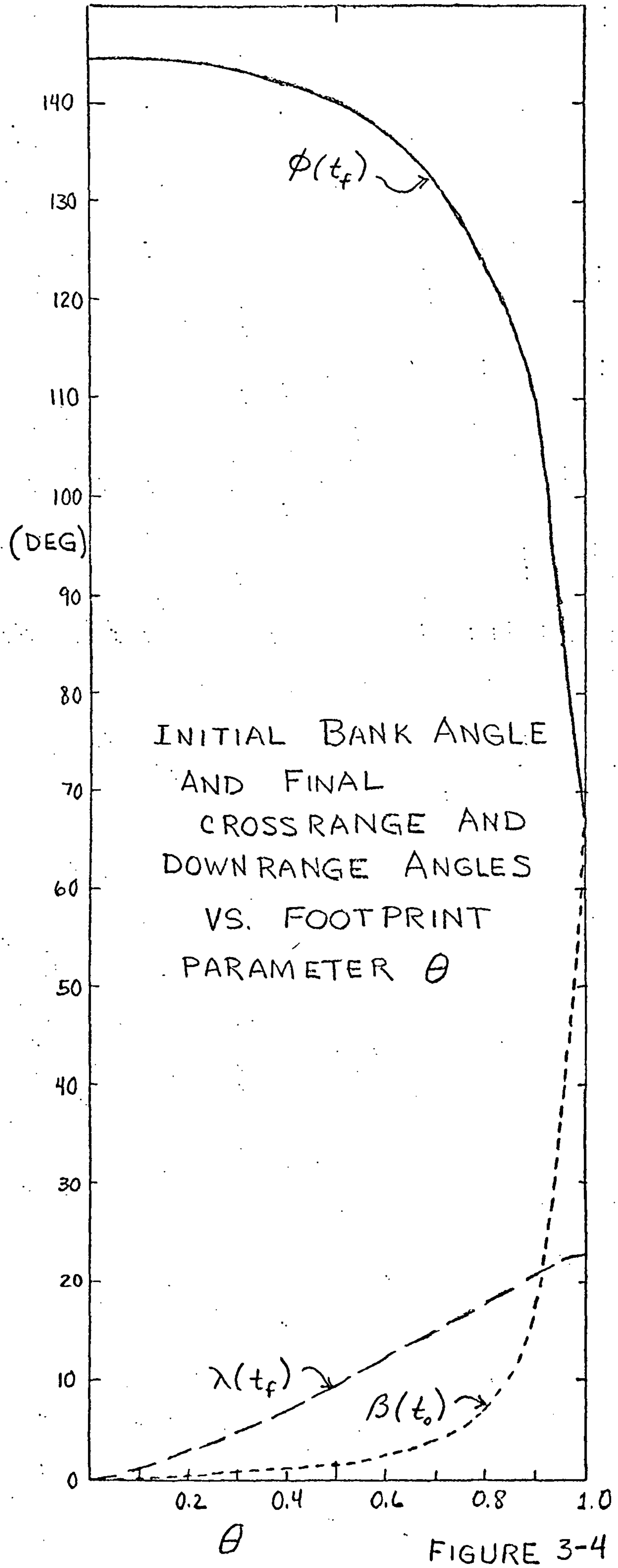
INITIAL BANK ANGLE AND FINAL CROSSRANGE AND DOWNRANGE ANGLES VS. FOOTPRINT PARAMETER θ
(DEG)
140
130
120
110
100
90
80
70
60
50
40
30
20
10
0
0.2
0.4
0.6
0.8
1.0
θ
$\phi(t_f)$
$\lambda(t_f)$
$\beta(t_o)$

FIGURE 3-4

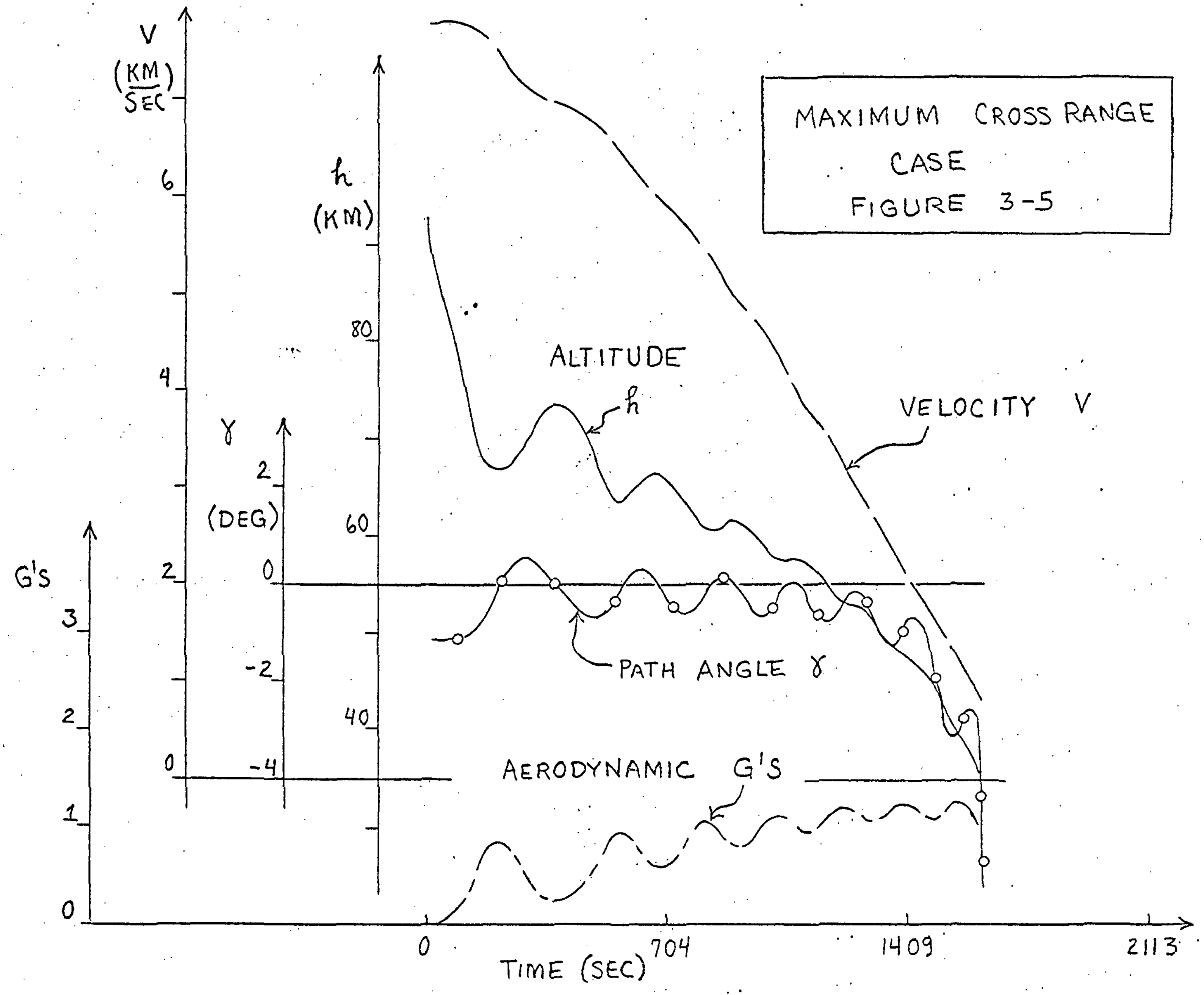

MAXIMUM CROSS RANGE CASE

FIGURE 3-5

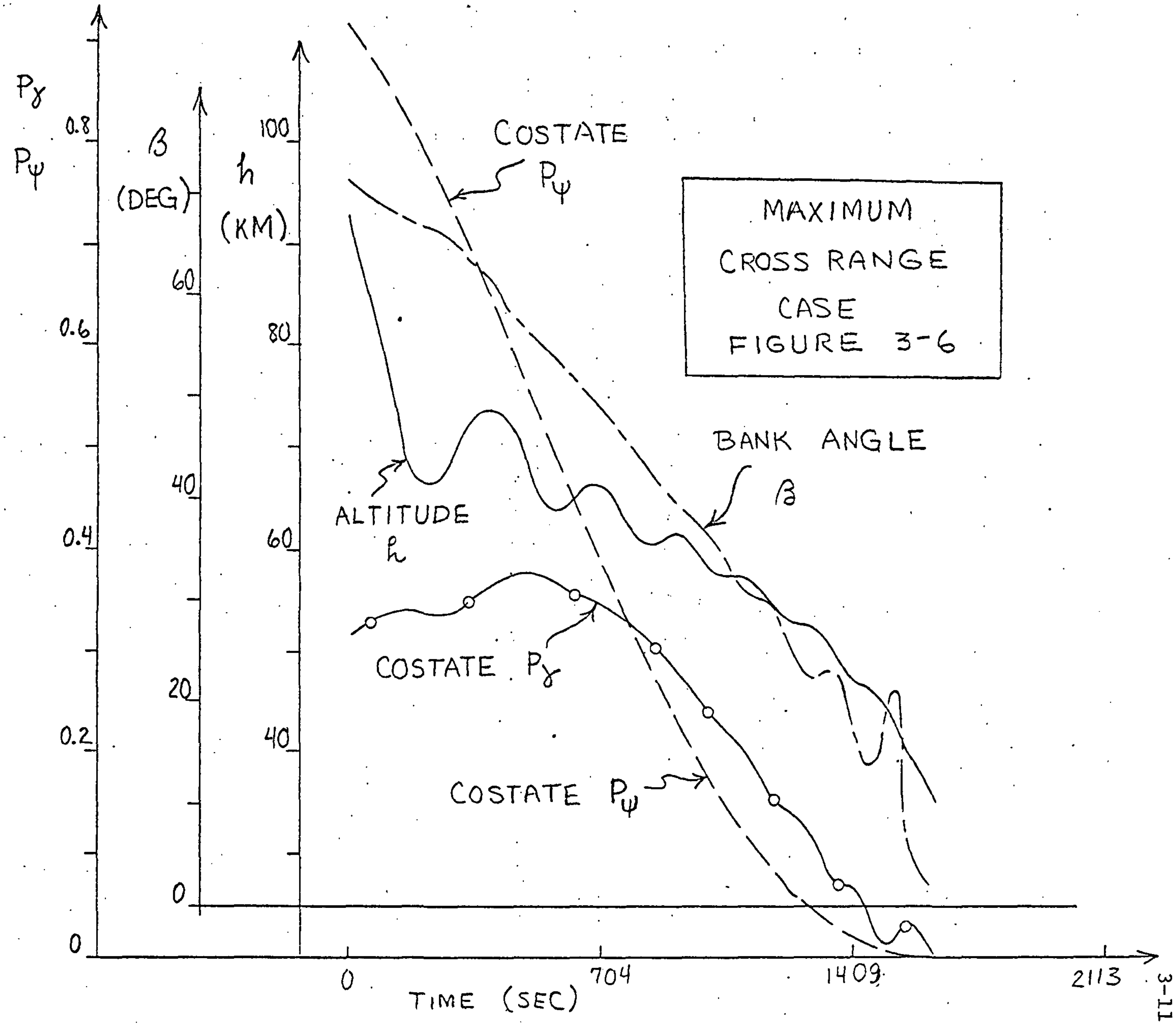

MAXIMUM
CROSS RANGE
CASE
FIGURE 3-6

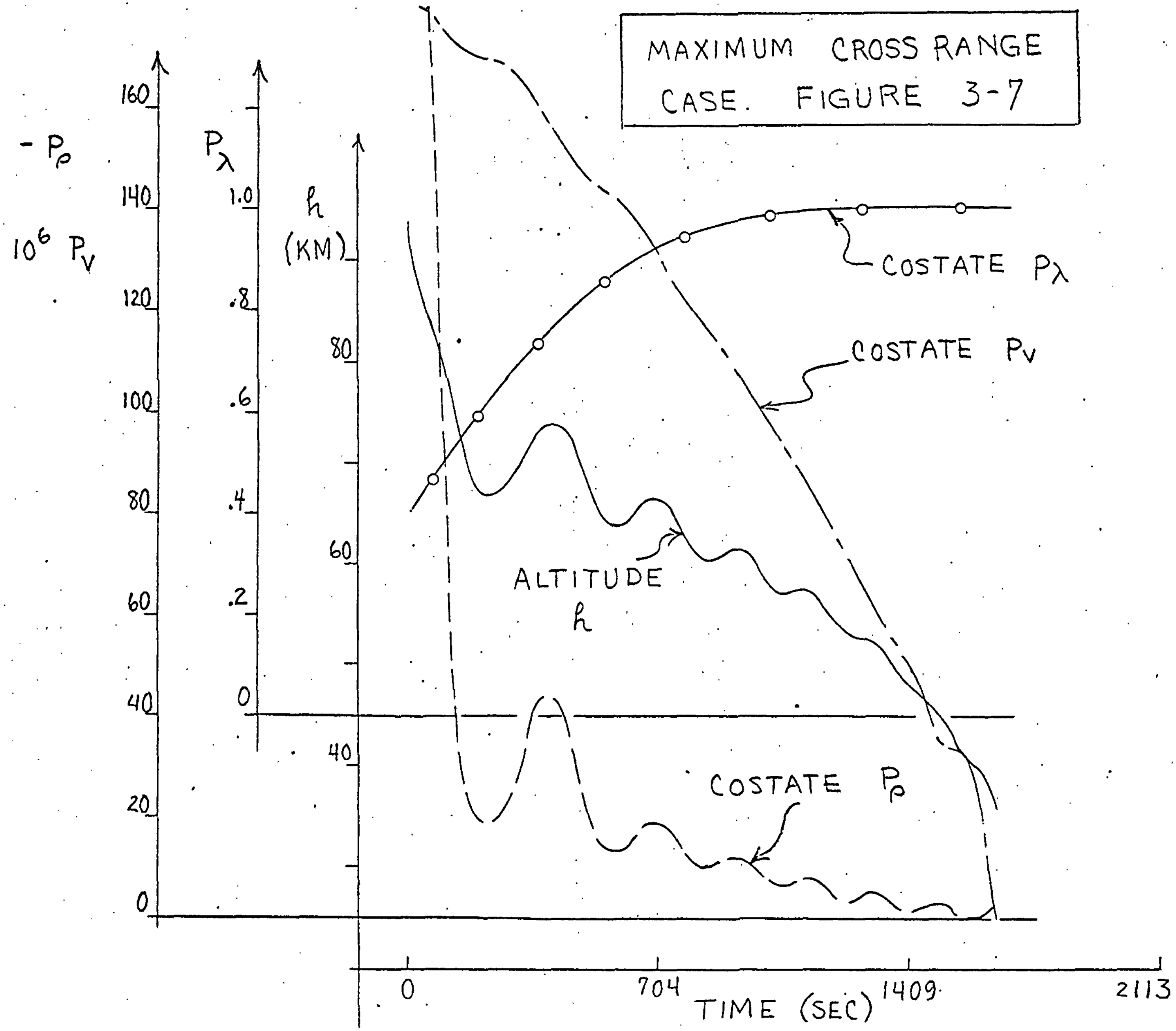

MAXIMUM CROSS RANGE CASE. FIGURE 3-7

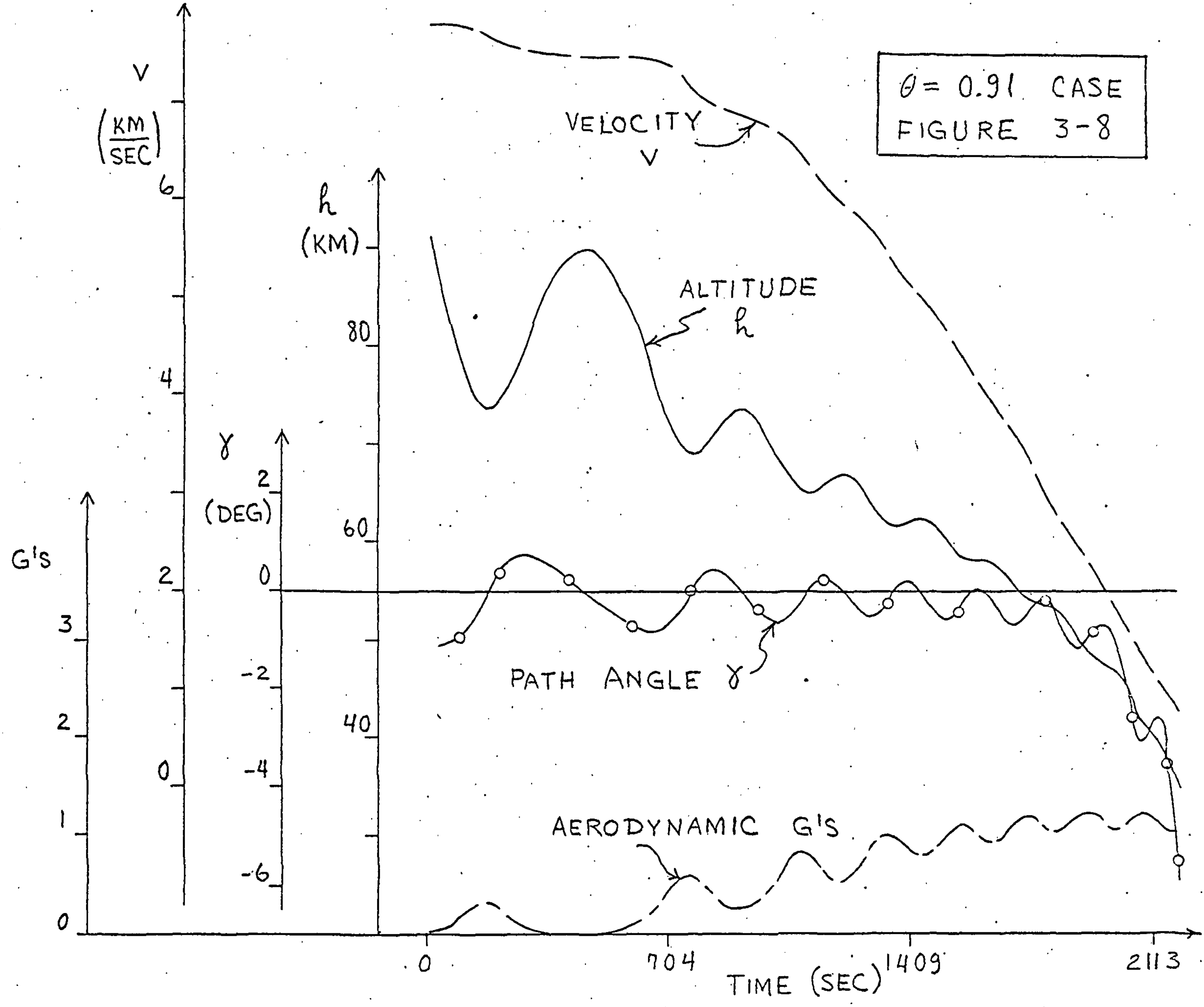
θ = 0.91 CASE
FIGURE 3-8

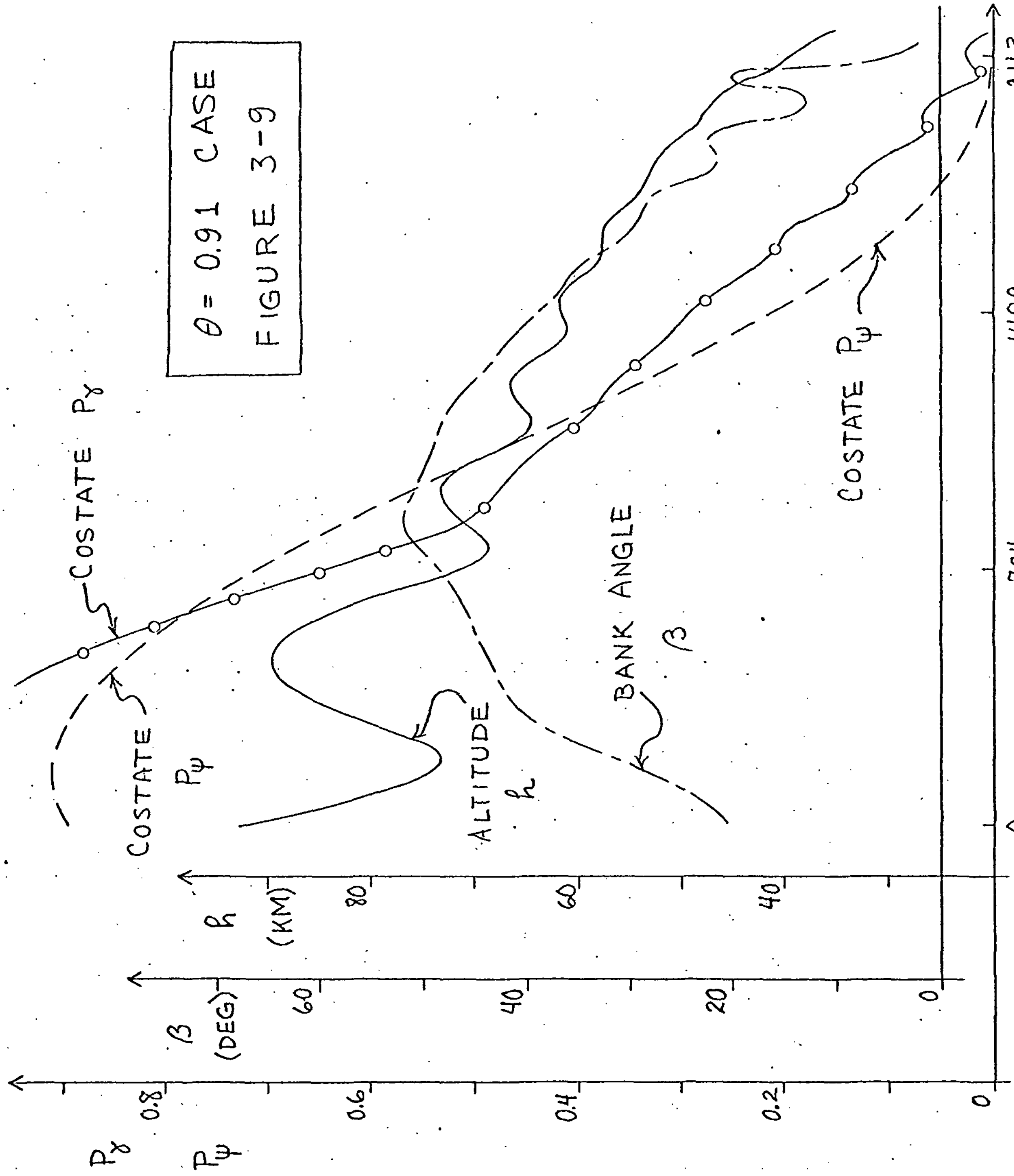

$\theta = 0.91$ CASE

FIGURE 3-9

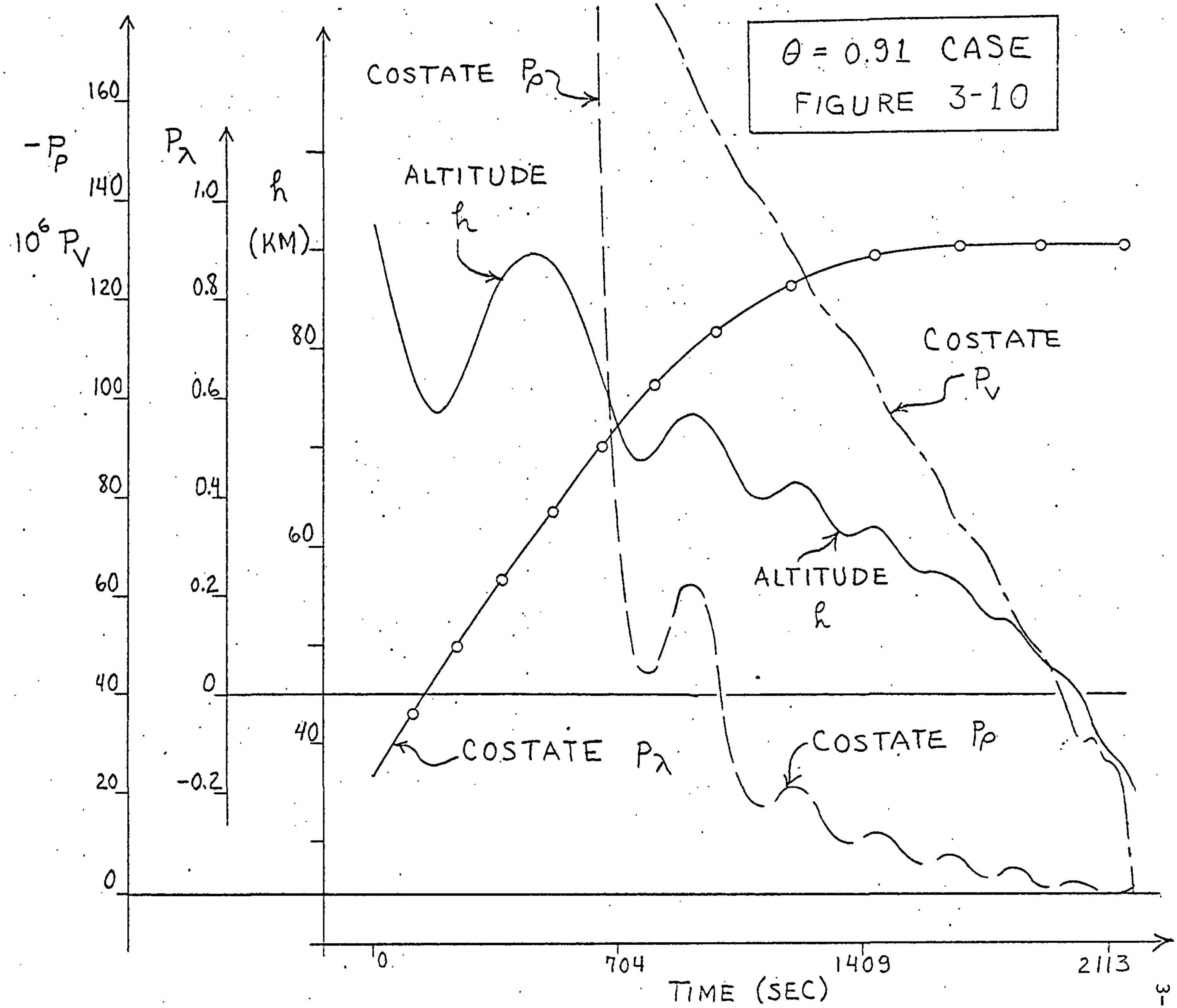

θ = 0.91 CASE
FIGURE 3-10

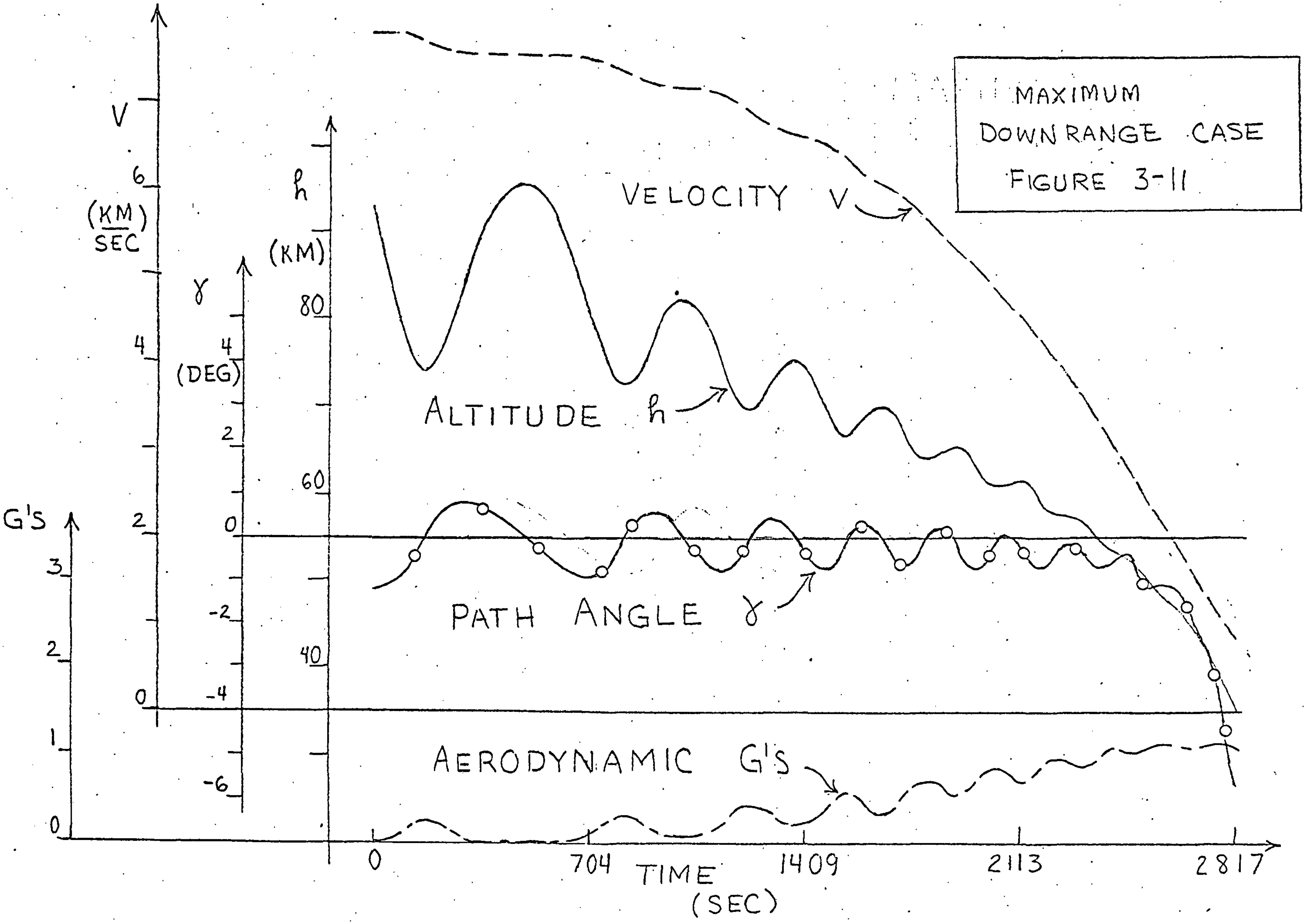

MAXIMUM DOWNRANGE CASE
FIGURE 3-11

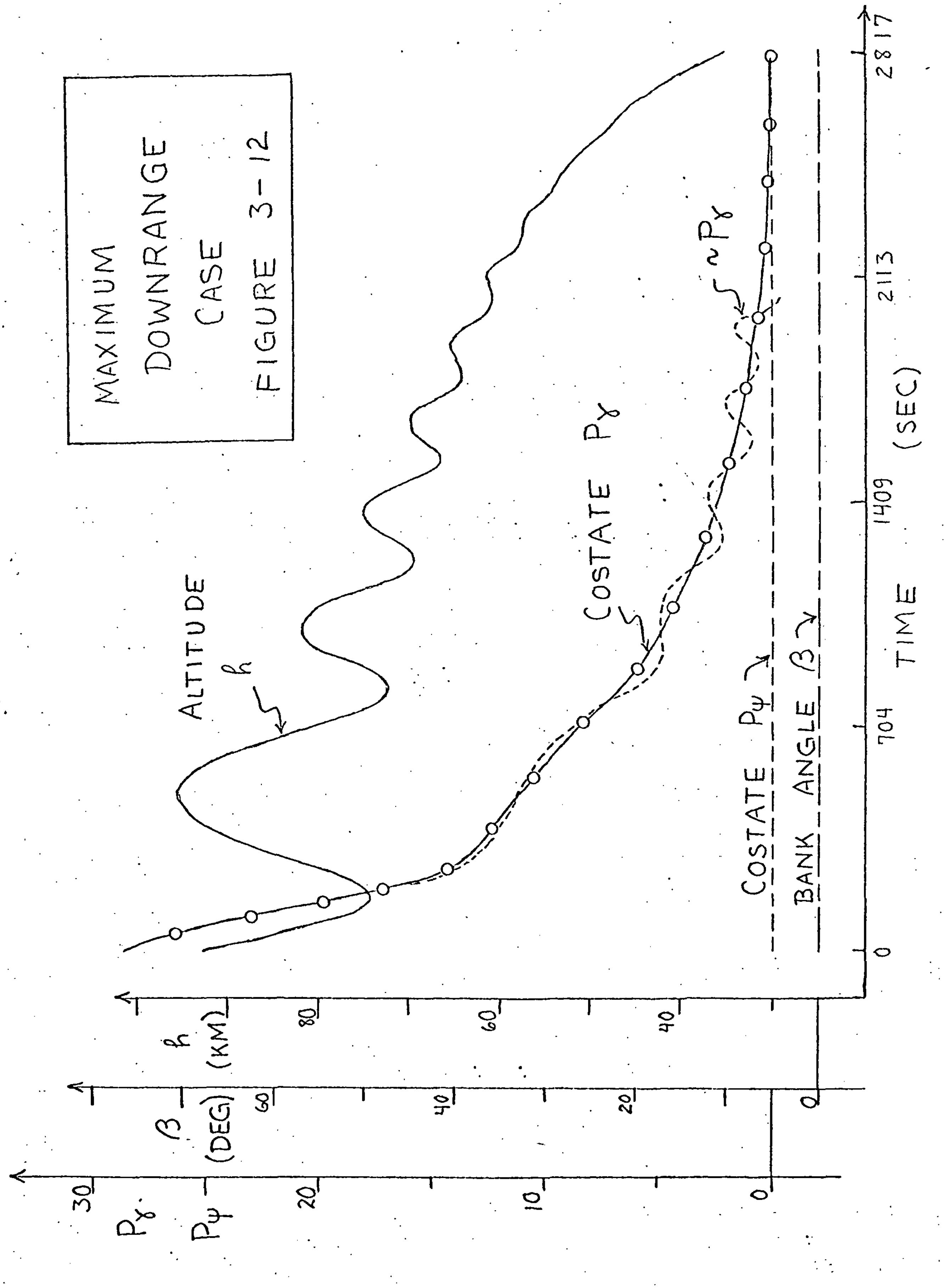

MAXIMUM DOWNRANGE CASE
FIGURE 3-12

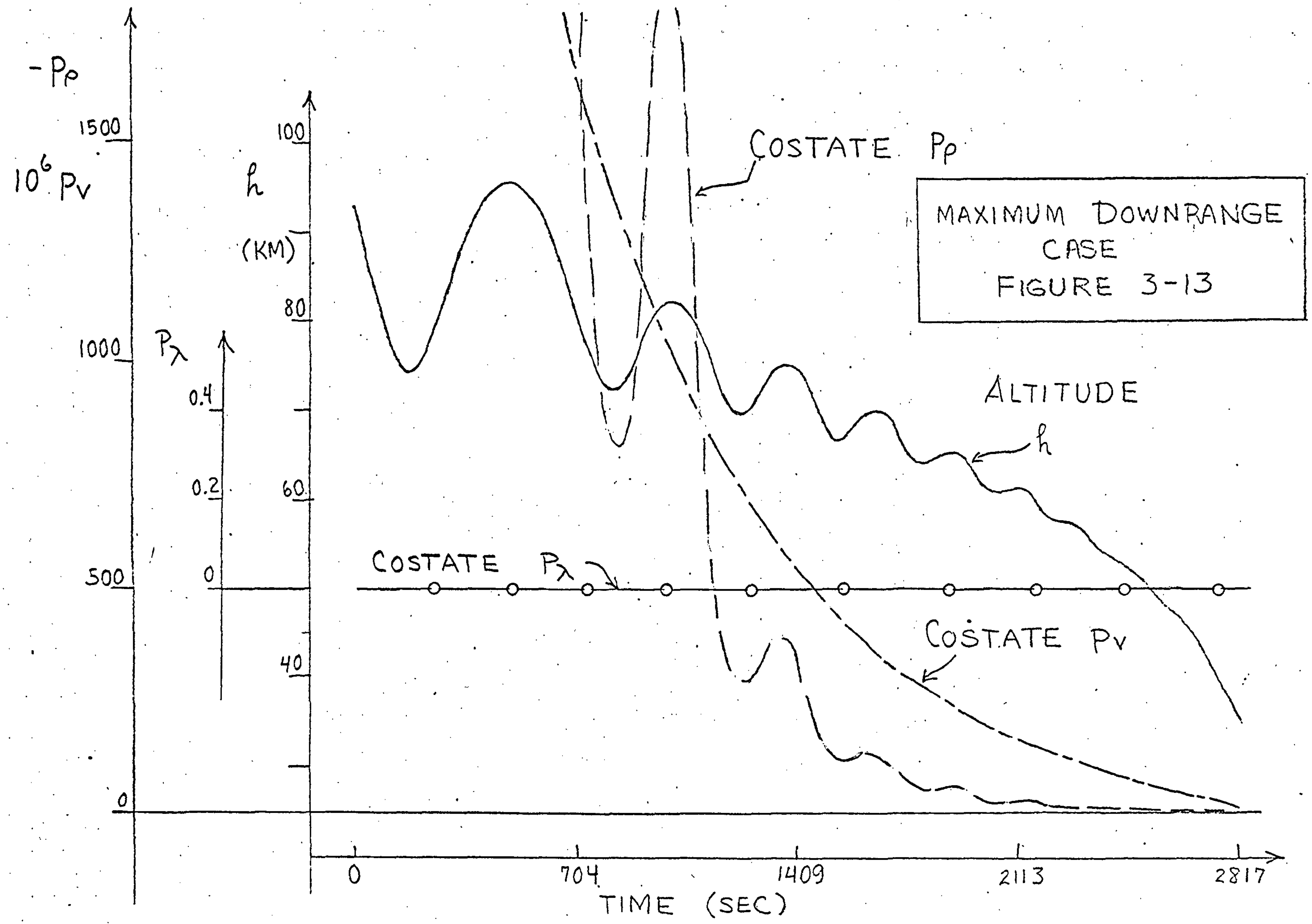

MAXIMUM DOWNRANGE CASE

FIGURE 3-13

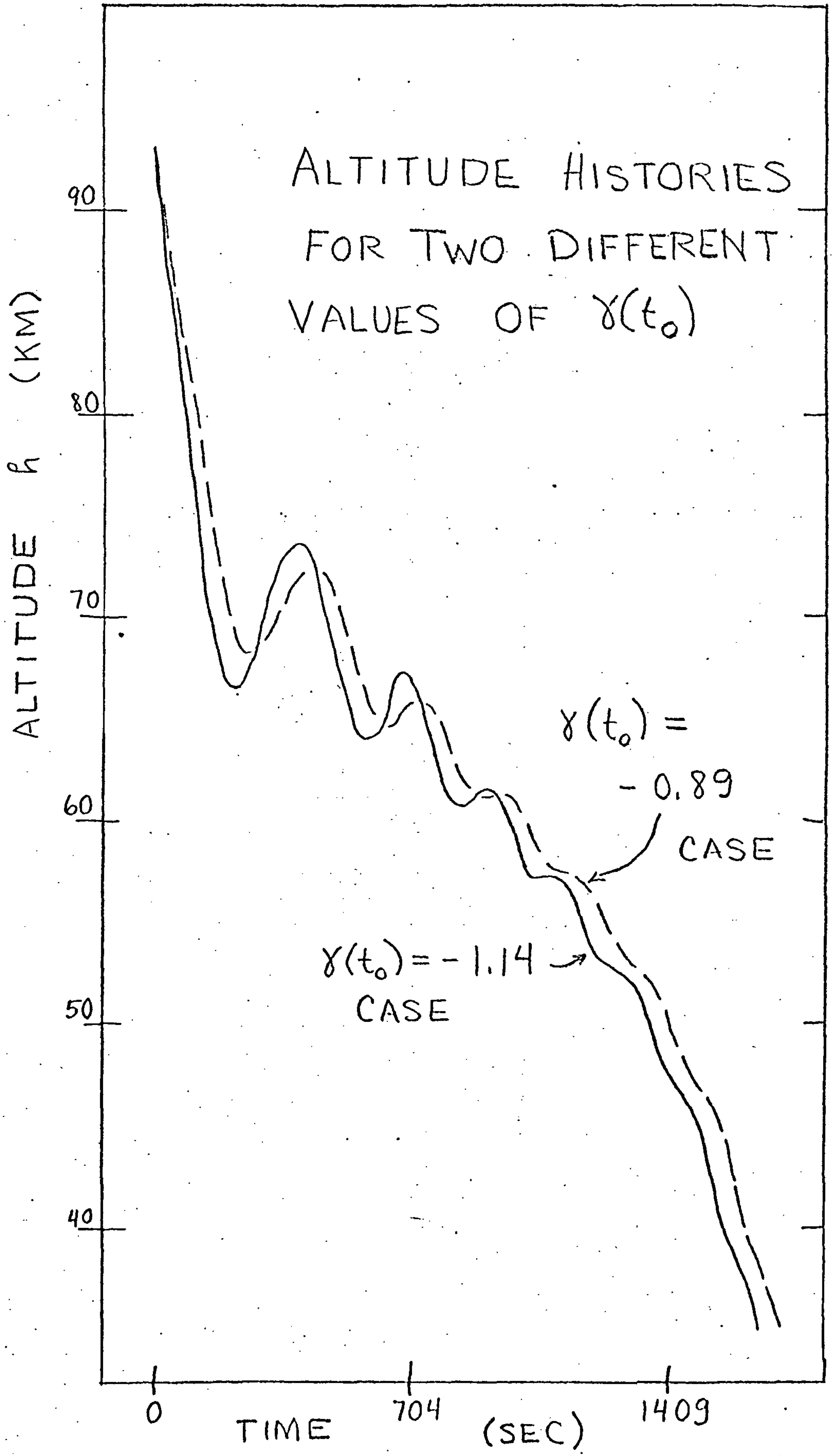
ALTITUDE HISTORIES FOR TWO DIFFERENT VALUES OF $\gamma(t_0)$
ALTITUDE h (KM)
90
80
70
60
50
40
$\gamma(t_0) = -0.89$ CASE
$\gamma(t_0) = -1.14$ CASE
0
704
1409
TIME (SEC)

FIGURE 3-14

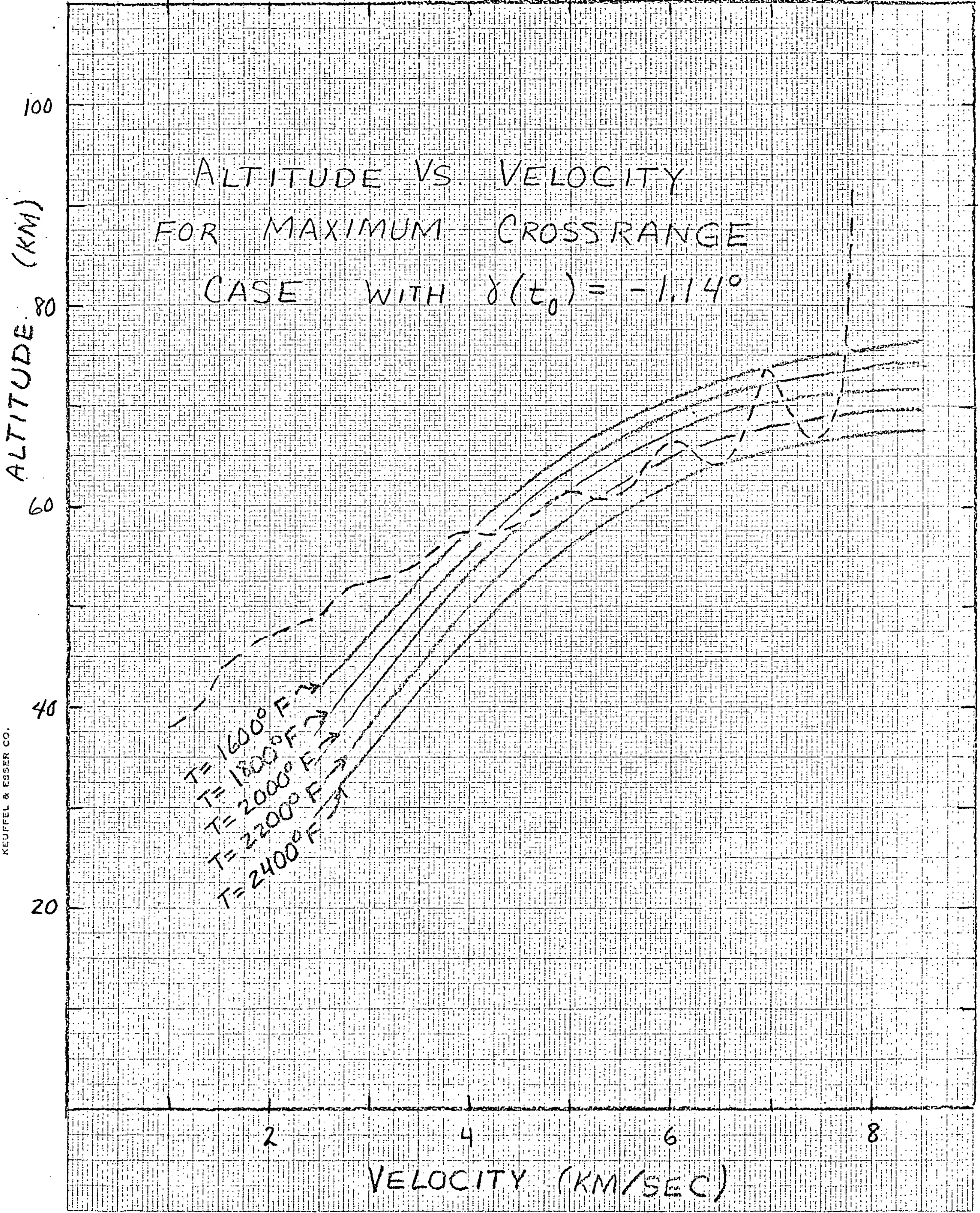
ALTITUDE VS. VELOCITY
FOR MAXIMUM CROSSRANGE
CASE WITH $\gamma(t_0) = -1.14°$
ALTITUDE (KM)
100
80
60
40
20
VELOCITY (KM/SEC)
2
4
6
8
T= 1600° F
T= 1800° F
T= 2000° F
T= 2200° F
T= 2400° F

FIGURE 3-15

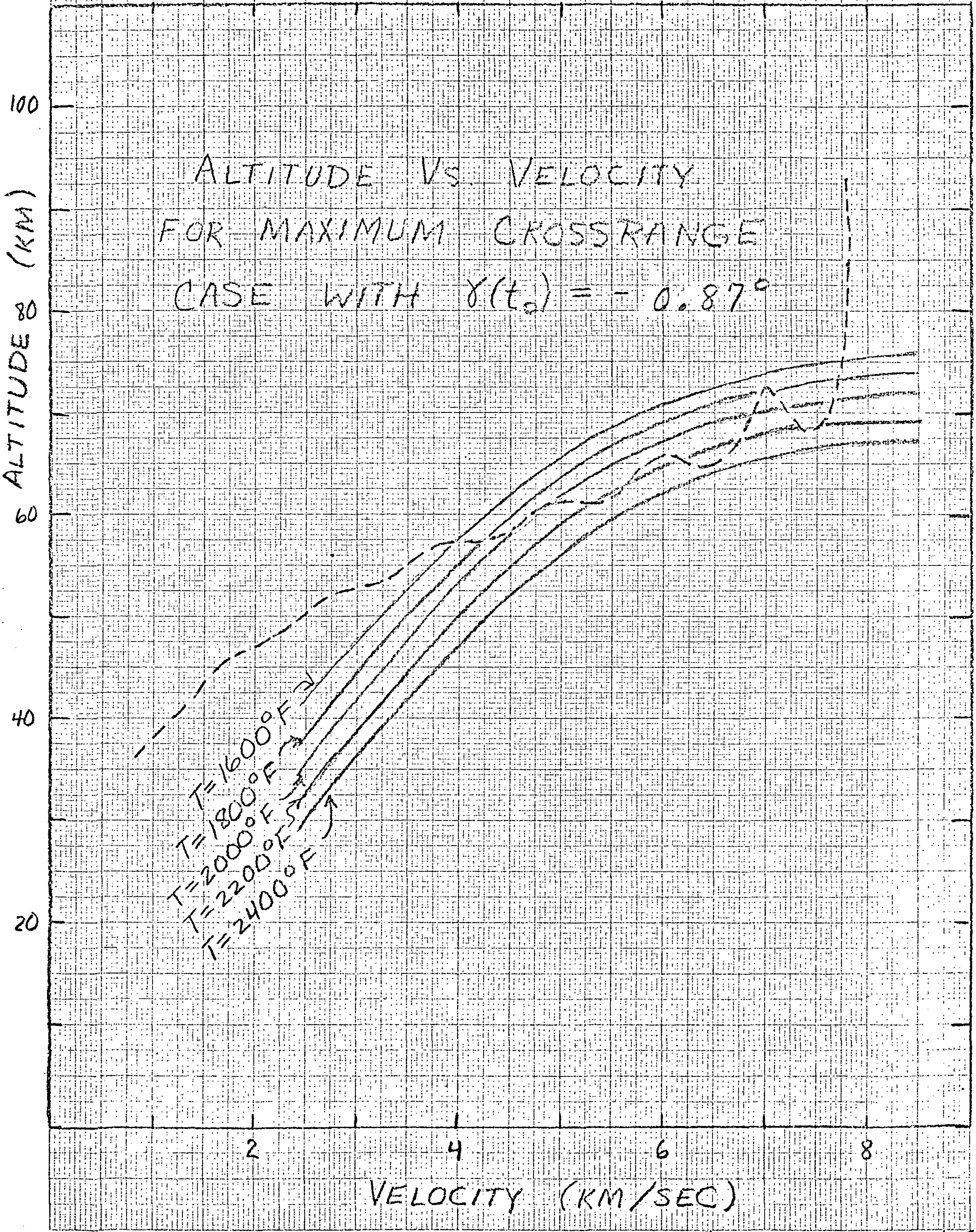
ALTITUDE VS VELOCITY
FOR MAXIMUM CROSSRANGE
CASE WITH $\gamma(t_o) = -0.87°$
ALTITUDE (KM)
100
80
60
40
20
2
4
6
8
VELOCITY (KM/SEC)
T=1600°F
T=1800°F
T=2000°F
T=2200°F
T=2400°F

FIGURE 3-16

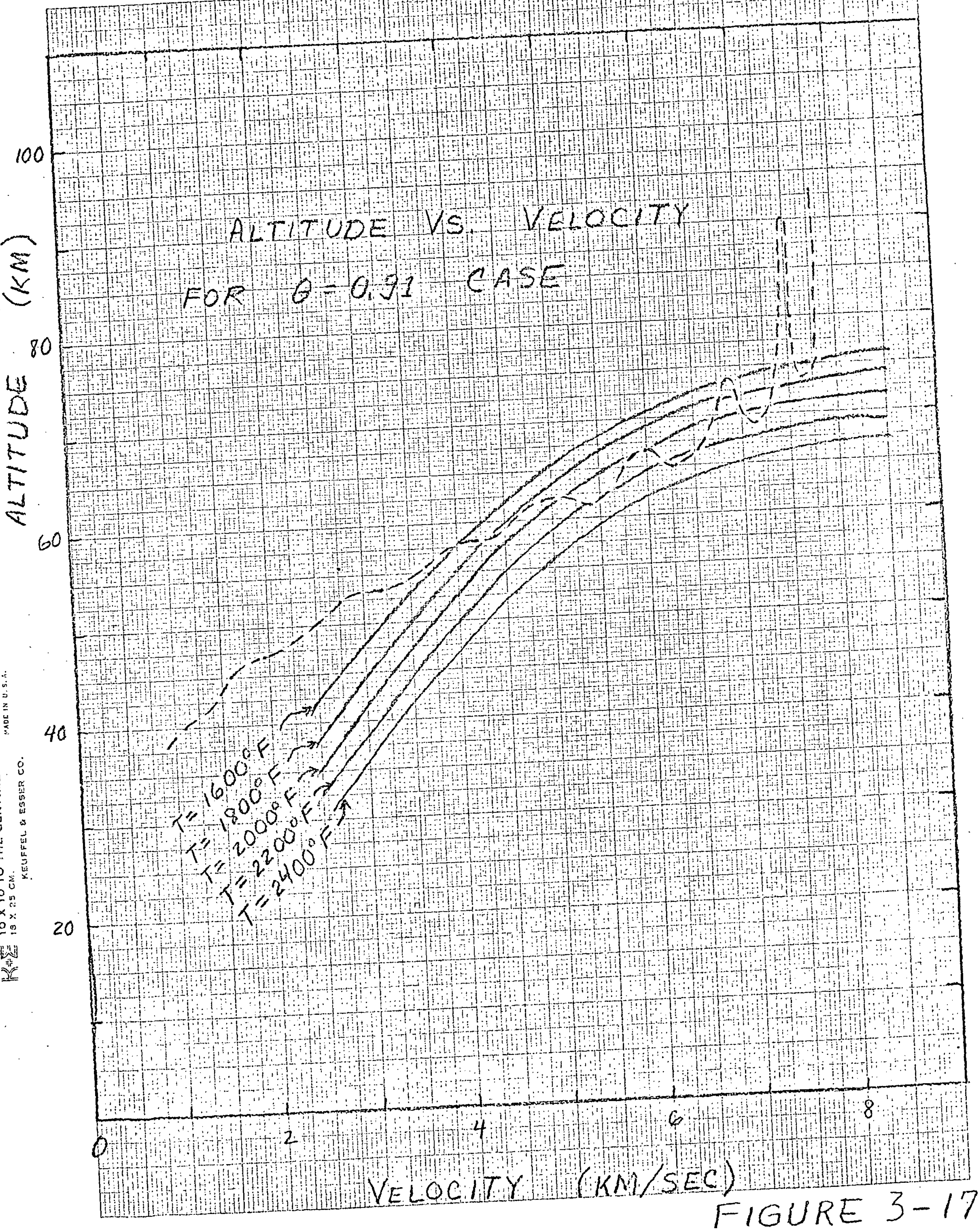
ALTITUDE VS. VELOCITY
FOR θ = 0.91 CASE
ALTITUDE (KM)
100
80
60
40
20
0
2
4
6
8
VELOCITY (KM/SEC)
T = 1600° F
T = 1800° F
T = 2000° F
T = 2200° F
T = 2400° F

FIGURE 3-17

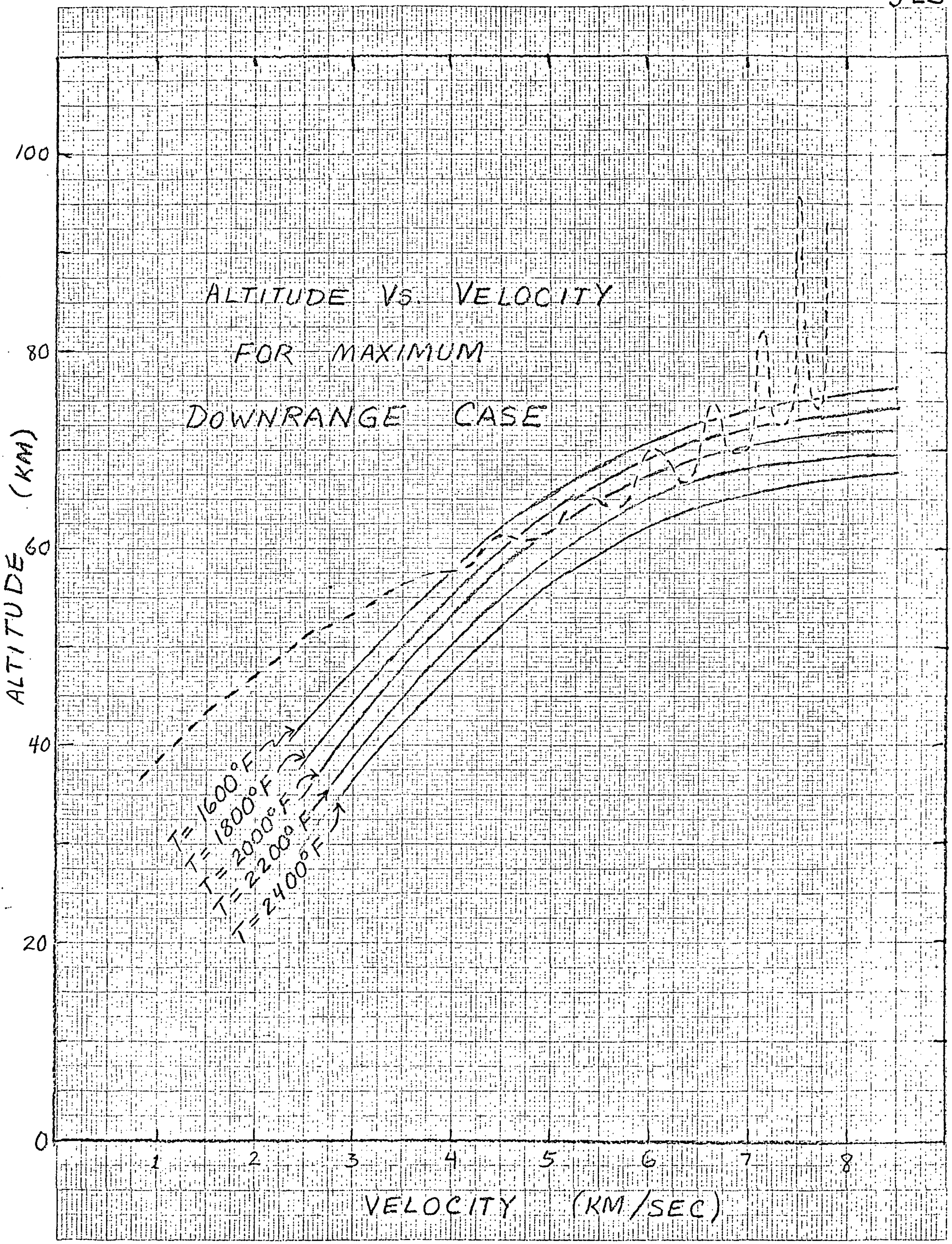
ALTITUDE Vs. VELOCITY
FOR MAXIMUM
DOWNRANGE CASE
ALTITUDE (KM)
VELOCITY (KM/SEC)
100
80
60
40
20
0
1
2
3
4
5
6
7
8
T = 1600°F
T = 1800°F
T = 2000°F
T = 2200°F
T = 2400°F

FIGURE 3-18

4. Generation of Reentry Trajectories Subject to In-Flight Constraints

The previous section discussed a method for determining a "footprint" by generating a sequence of trajectories which are not subject to in-flight constraints and which are optimal in the sense that equation 3-1 is maximized subject to a given terminal altitude. Here we discuss a method, motivated by reference 4, of generating trajectories which are not necessarily optimal in any sense subject to in-flight constraints.

These trajectories have constant angle of attack with roll angle free and satisfy constraints on maximum total aerodynamic acceleration and maximum heating rate. The method we use to generate them is summarized in the following:

1) Entry is at a constant bank angle from deboost until the maximum permissible heating rate is obtained. This bank angle is uniquely determined by imposing the requirement that the time derivative of heating-rate be zero when the heating rate limit is encountered. This "tangency condition" is necessary to avoid violating the constraint.

2) Constant heating rate is then maintained by varying bank angle.

3) At the appropriate time, a transition is made from constant heating-rate flight to constant aerodynamic acceleration flight by maintaining a constant bank angle for 60 seconds. The timing of the transition maneuver and the angle of bank are uniquely determined by applying the appropriate tangency condition at the beginning of the constant dynamic pressure arc.

4) Constant aerodynamic acceleration is maintained by varying bank angle until a heading of ±90° is obtained.

5) Bank angle is then held at zero for the remainder of the flight. This strategy is at least locally optimal with respect to maximizing cross range after a heading angle of ±90° is attained.

For a given initial orbit, the family of trajectories generated using this technique is parameterized by deboost time, deboost velocity increment, maximum heating rate and maximum aerodynamic acceleration. Subject to obvious limits, these parameters may be regarded as mission variables selected to provide suitable trajectory shaping for each mission.

Following reference 3, we have assumed that heating rate is proportional to $\rho^{1/2} v^3$. For a particular vehicle, actual heating rate at any point on the vehicle will vary with angle of attack and will almost surely be a more complicated function of vehicle state. However, we believe that this simple model is adequate for the purpose of investigating the feasibility of trajectory shaping techniques and guidance algorithms. Moreover, the simple model can be made to at least crudely approximate more sophisticated models by the selection of an appropriate constant of proportionality.

The data presented in figures 4-1 through 4-3 illustrate a typical trajectory generated by the technique just described. The 2300°F boundary, appearing as a dashed line in figure 4-2, was taken from reference 3. Maximum temperature occurs during the transition and is clearly an increasing function of both maximum heating rate and maximum aerodynamic acceleration.

If we superimpose figure 4-2 and figure 3-15, which is a plot of altitude versus velocity for an unconstrained optimal trajectory which maximizes cross-range, the suggestive result is figure 4-4. The trajectory of figure 4-2 seems to be a "smoothed" version of the optimal trajectory. Moreover, not much cross-range is lost as a result of the smoothing process since the non-optimal trajectory terminates at a final crossrange of 20.8° whereas the optimal trajectory terminates at 22.7°. It is possible to obtain even more crossrange by adjusting the parameters of the non-optimal trajectory properly (cf. point 5 of figure 3-1). This result suggests that trajectories generated by the technique described in this section are perhaps nearly optimal with respect to final cross-range. We are presently investigating the possibility of taking advantage of this property in a practical guidance algorithm.

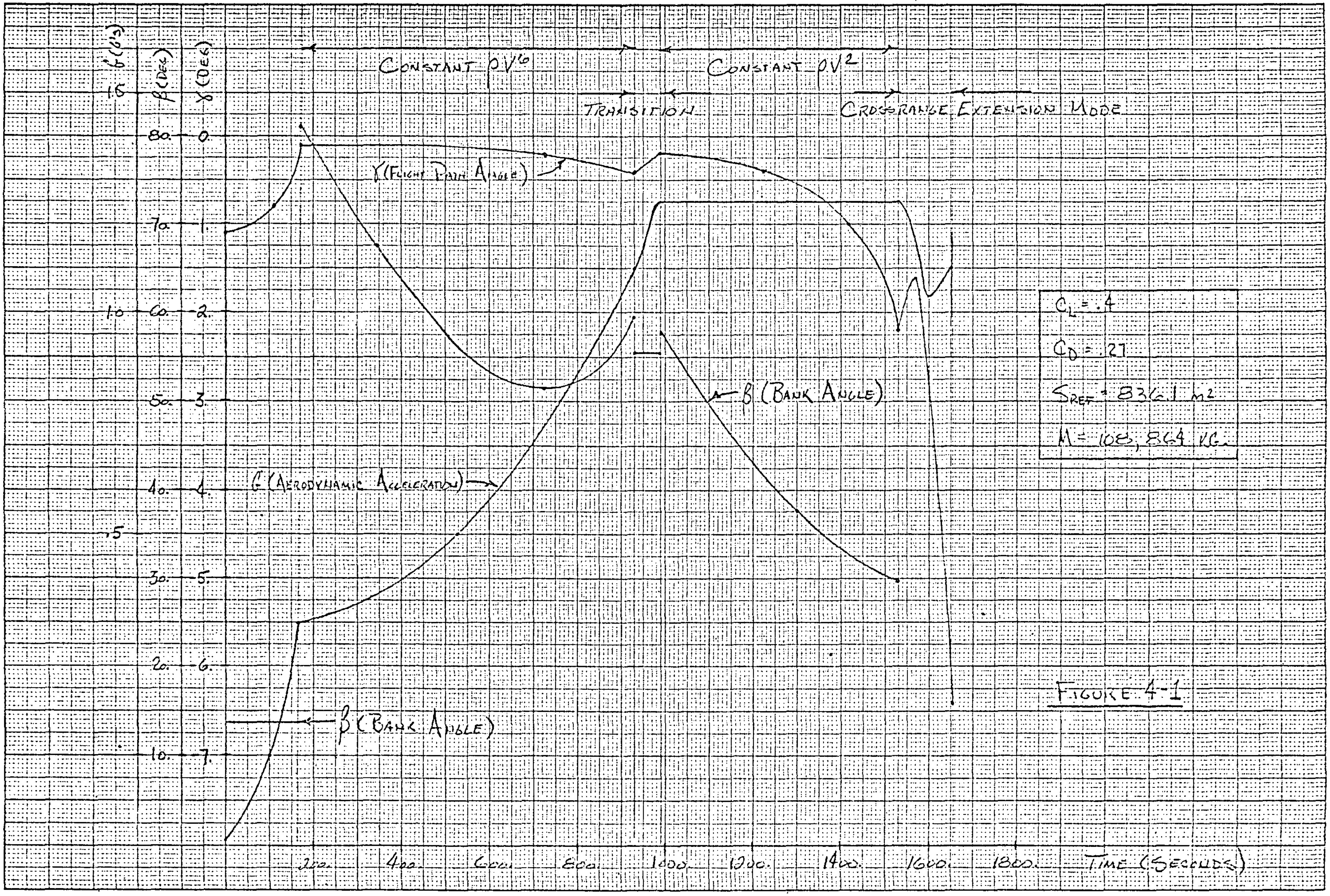
G (G's)
β (DEG)
γ (DEG)
1.5
80
0
70
1
1.0
60
2
50
3
40
4
.5
30
5
20
6
10
7
CONSTANT ρV⁶
CONSTANT ρV²
TRANSITION
CROSSRANGE EXTENSION MODE
γ (FLIGHT PATH ANGLE)
G (AERODYNAMIC ACCELERATION)
β (BANK ANGLE)
β (BANK ANGLE)
C_L = .4
C_D = .27
S_REF = 836.1 m²
M = 108,864 KG
200
400
600
800
1000
1200
1400
1600
1800
TIME (SECONDS)

FIGURE 4-1

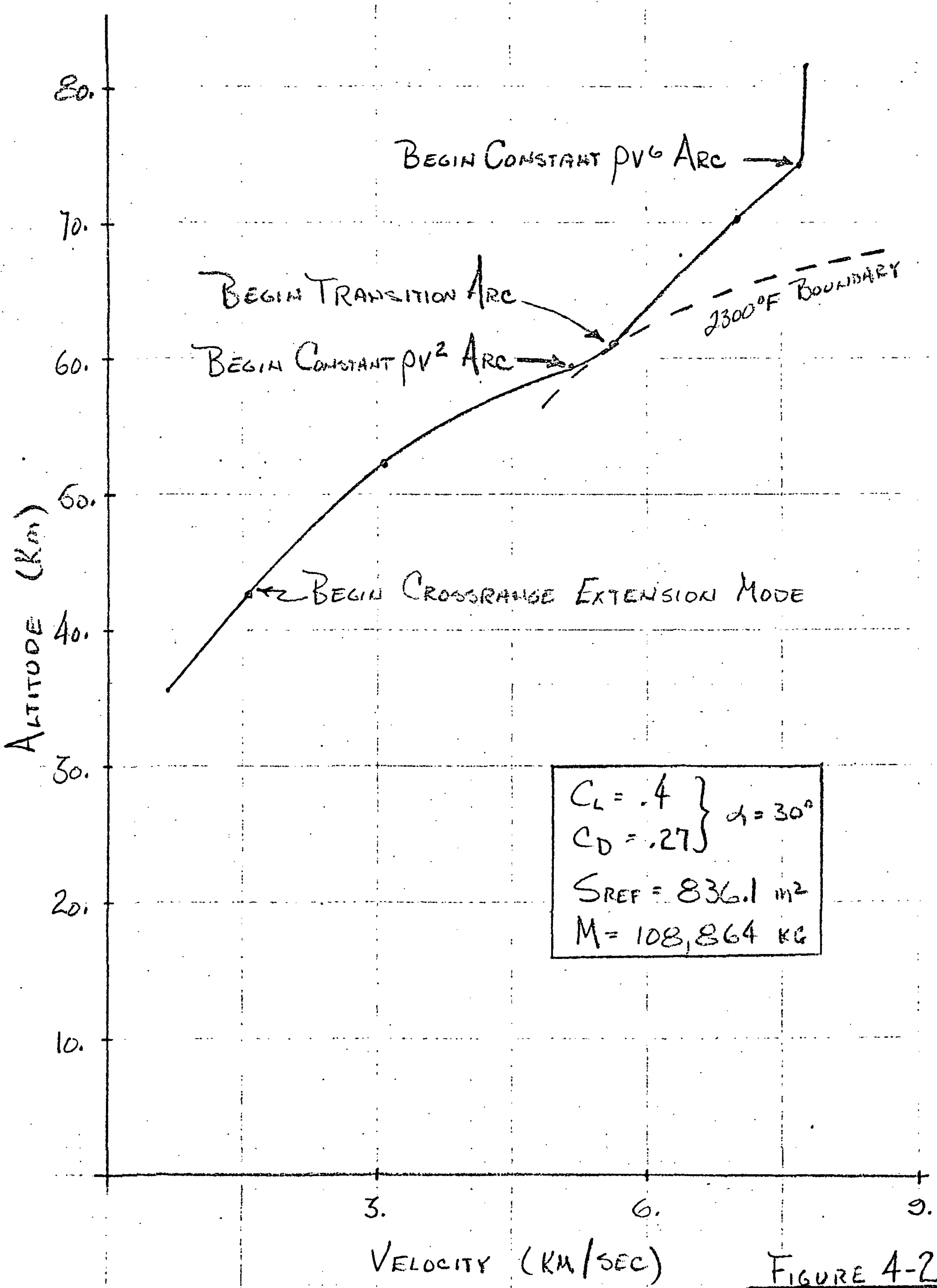
80.
70.
60.
60.
40.
30.
20.
10.
Altitude (Km)
3.
6.
9.
Velocity (Km/sec)
Begin Constant ρV⁶ Arc
Begin Transition Arc
Begin Constant ρV² Arc
2300°F Boundary
Begin Crossrange Extension Mode
C_L = .4
C_D = .27
α = 30°
S_REF = 836.1 m²
M = 108,864 kg

Figure 4-2

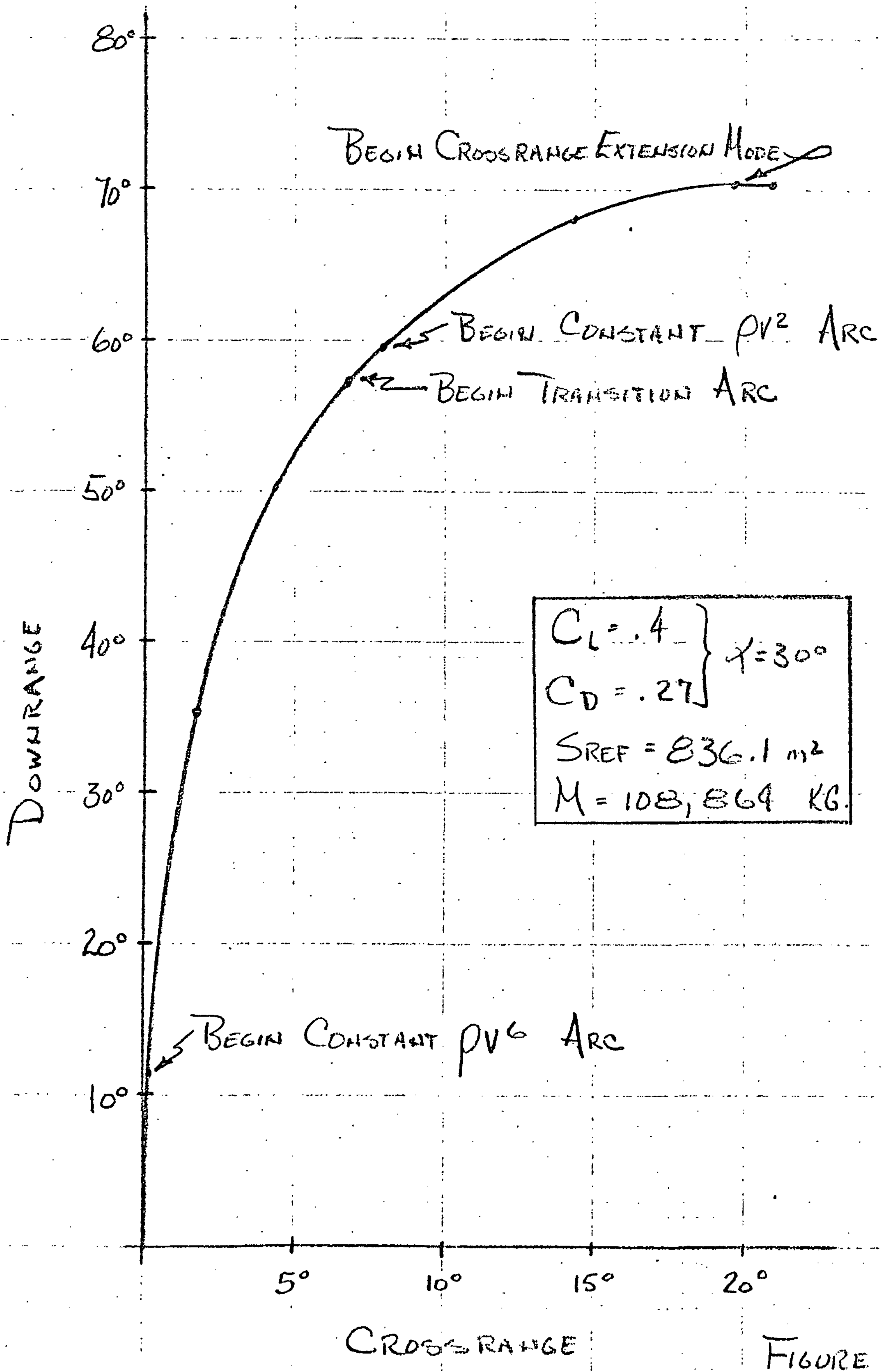

80°
70°
60°
50°
40°
30°
20°
10°
DOWNRANGE
5°
10°
15°
20°
CROSSRANGE
BEGIN CROSSRANGE EXTENSION MODE
BEGIN CONSTANT ρV² ARC
BEGIN TRANSITION ARC
BEGIN CONSTANT ρV⁶ ARC
C_L = .4
C_D = .27
α = 30°
S_REF = 836.1 m²
M = 108,864 KG

FIGURE 4-3

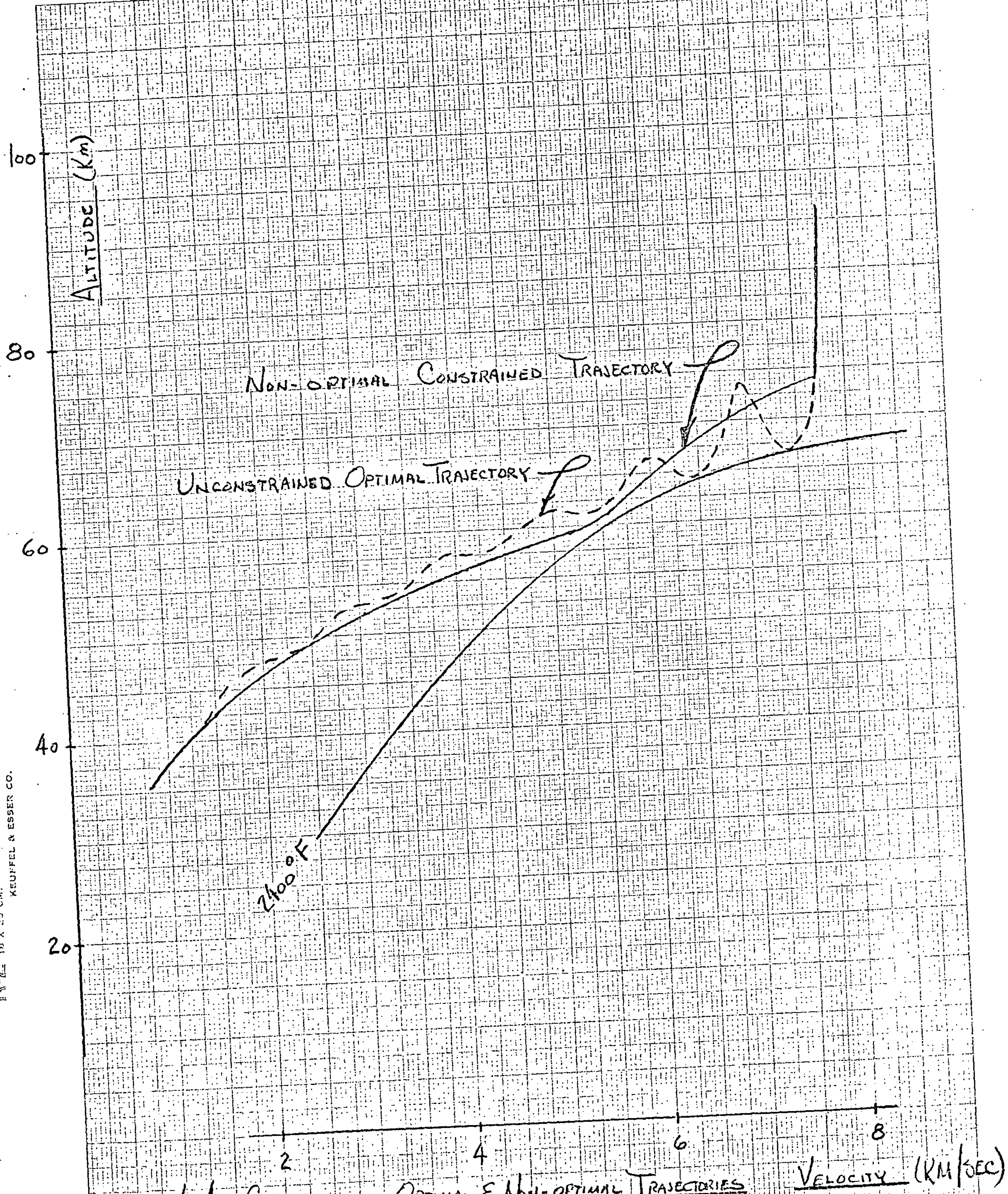

FIGURE 4.4. COMPARISON OF OPTIMAL & NON-OPTIMAL TRAJECTORIES

5. Summary of Work and Conclusions

Early work under this contract concerned minimum-fuel vacuum ascent to orbit and transfer between orbits. This work is summarized in [5]. Many of the numerical techniques currently used in the GUIDE program [6] were first developed under this contract. Work on shuttle optimal atmospheric ascent is summarized in [7]. Work on reentry trajectories is presented in this current Report.

A result which we consider particularly significant is that the trajectory described in Section 4, which consists almost entirely of arcs with ρv^6 constant or ρv^2 constant, achieves almost the same crossrange as the optimal unconstrained trajectory, and has no oscillation in altitude or flight path angle except during the final unconstrained range extension mode. It is suggestive that the non-optimal constrained trajectory follows a path in altitude-velocity space (Fig. 4-4) which is a smoothed version of the altitude-velocity path of the optimal unconstrained trajectory.

We have observed that unconstrained optimal trajectories are difficult to converge and we have observed that a trajectory which is not optimal in any sense can achieve near optimal crossrange. Our experience with the trajectory described in Section 4 suggests that, for trajectories with constant angle of attack, it may be fruitful to choose β to maintain flight in various mainfolds of the form $f(\rho,v)$ = constant. These mainfolds may be chosen to be the mean of oscillatory optimal paths in ρ,v. Crossrange would be determined by switching the sign of β.

The fact that by following the heating rate constraint one eliminates the oscillation in h and γ suggests the possibility that an optimal arc subject to a heating rate constraint might be considerably less oscillatory than the unconstrained optimal arc, and might be easier to converge. A guidance scheme might then consist of flying an optimal maximum crossrange trajectory subject to a heating constraint until such time as the trajectory, is continued with $\beta = 0$, would pass over the target. The remainder of the trajectory would consist of maneuvers to lose altitude by rolling symmetrically about $\beta = 0$.

References

1. Progress Report for December, 1971.

2. W.H.T. Loh et al. "Reentry and Planetary Entry Physics and Technology," Volume I (book), Springer-Verlag, New York, 1968.

3. Letter, J.A. Forney, Thermal Environment Branch, S&E-AERO-AT, NASA Marshall Space Flight Center, Huntsville, Alabama, to David Winfield, IBM Corporation, Cambridge, Mass., August 3, 1971. Subject: Orbiter Temperature Boundaries.

4. Memorandum, from EX/Chief, Engineering Analysis Division, NASA Manned Spacecraft Center, Houston, Texas, January 6, 1972. Subject: Typical Mark I/II Orbiter Reentry Trajectories.

5. K.R. Brown, E.F. Harrold, and G.W. Johnson, "Rapid Optimization of Multiple-Burn Rocket Trajectories," NASA Contractors Report CR-1430, September 1969. Also presented at the 20th Congress of the I.A.F. at Mar Del Plata, Argentina, October 1969.

6. A.O. Cohen, "GUIDE 71/6 Program Documentation" IBM Federal Systems Division, Burlington, Mass., under Contract NAS 8-24018, October 14, 1971.

7. K.R. Brown, E.F. Harrold, G.W. Johnson, "Some New Results on Space Shuttle Atmospheric Ascent Optimization", AIAA Paper No. 70-978, August 1970.

A1 -- Vehicle Aerodynamic Coefficient Model, Atmospheric Density Model and Initial State Data

We have devised a four-parameter model for C_L and C_D given by

$$\begin{aligned} C_L(\alpha) &= C_{Lmax} \sin 2(\alpha-\zeta) \\ C_L(\alpha) &= C_{Do} + \frac{1}{2} C_{Dmax} [1 - \cos 2(\alpha-\zeta)] \end{aligned} \tag{A1-1}$$

In figure A1-1, C_L and C_D as given by these formulas are compared with more exact data taken from [1].

Atmospheric density, ρ, is computed according to an exponential model as

$$\rho = \rho_o e^{-k(r-r_o)} \tag{A1-2}$$

where r_o = earth's radius. We are interested mainly in altitudes from 35 km. to 100 km. and have chosen ρ_o and k to give a good approximation to atmospheric density at these altitudes. A comparison of atmospheric density computed according to the formula (A1-2) and the density of the 1962 U.S. Standard Atmosphere is given in figure A1-2.

The initial vehicle state and vehicle characteristics used for generating all the numerical data appearing in this report are given in table A1-1.

---

[1] Letter from Mr. Jerome R. Redus of George C. Marshall Space Flight Center, S&E-AERO-GT, to Dr. G. W. Johnson of IBM, June 1, 1970.

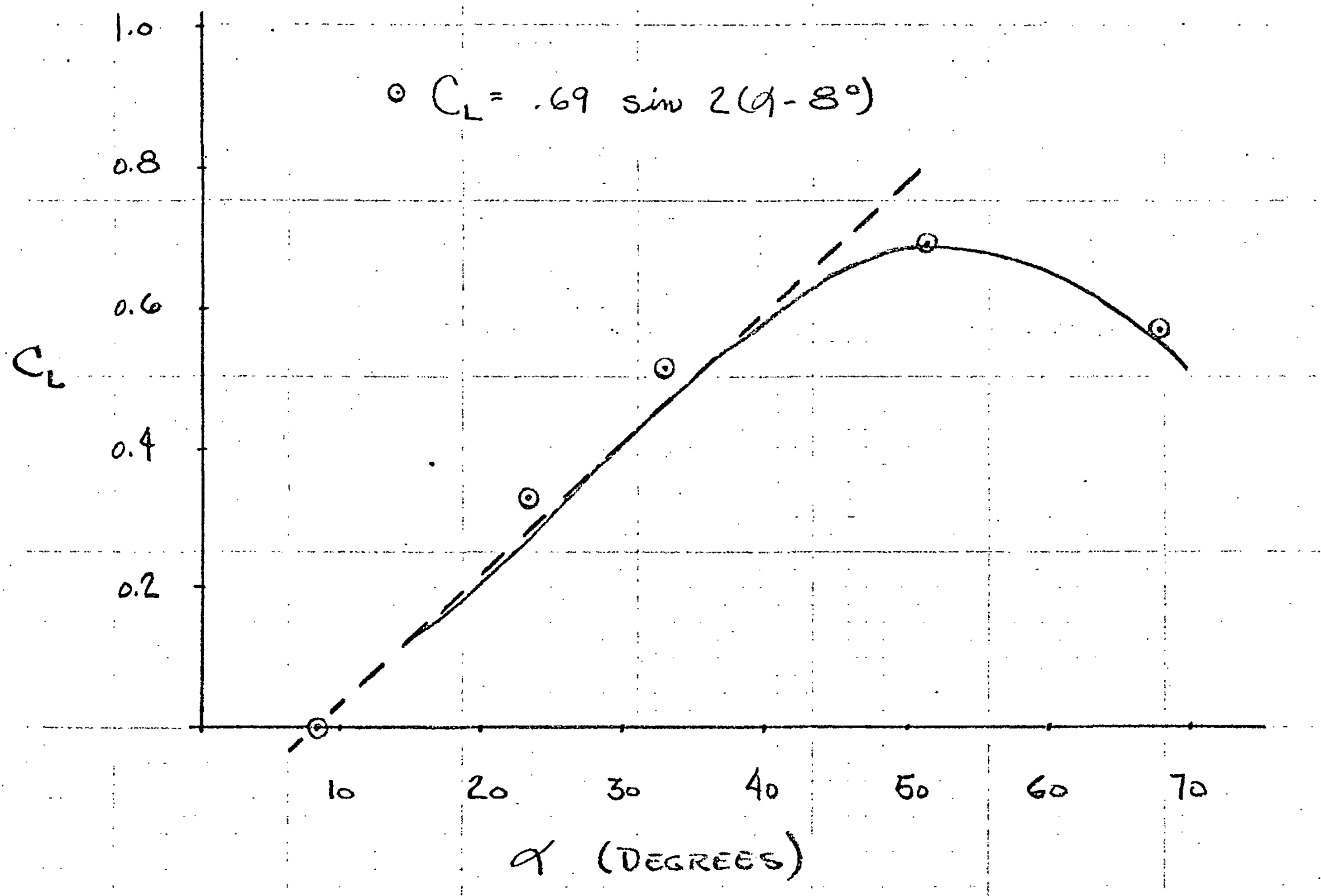

FIGURE A1-1(A) HYPERSONIC LIFT COEFFICIENT VERSUS ANGLE OF ATTACK

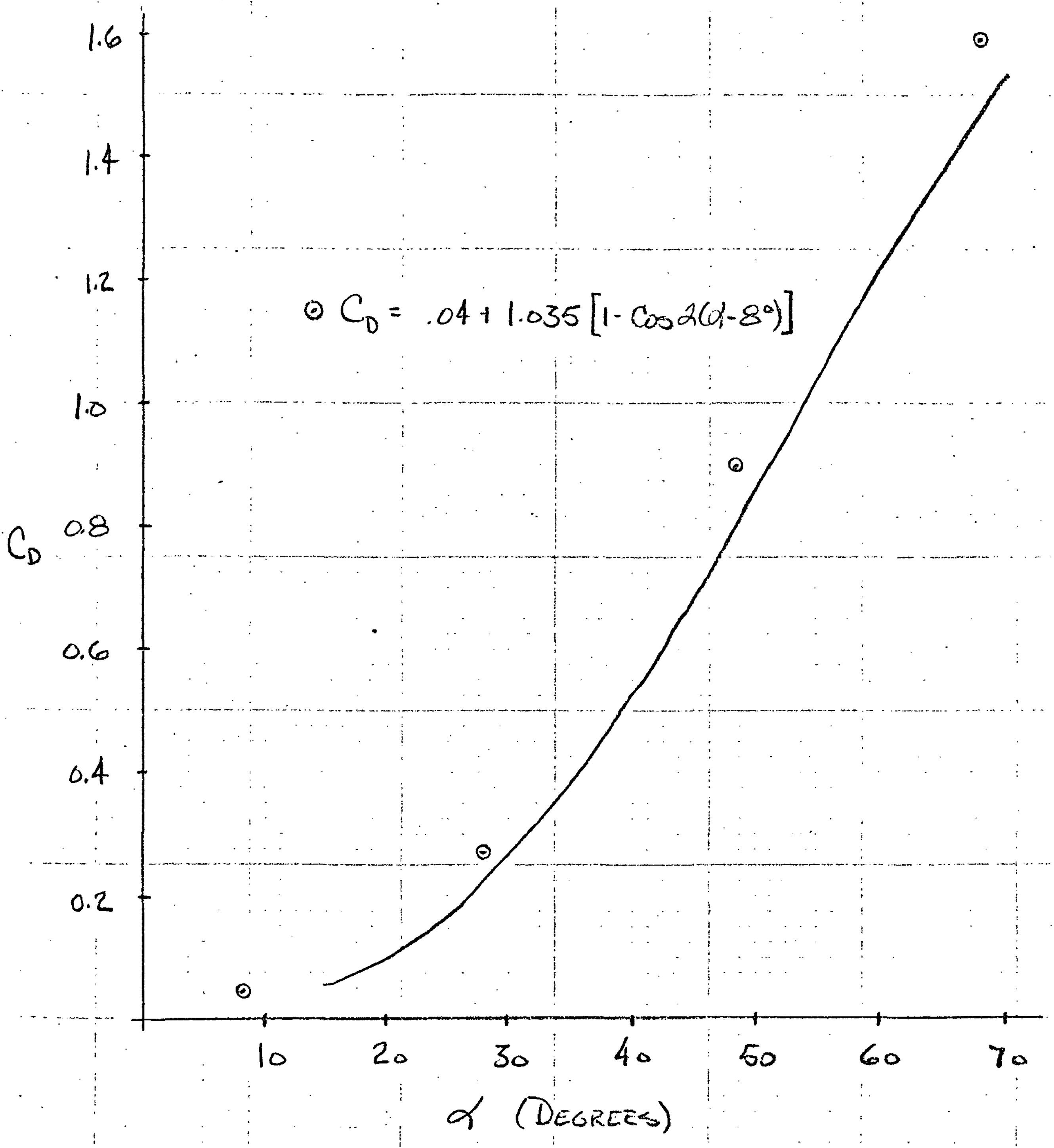

FIGURE A1-1(B) HYPERSONIC DRAG COEFFICIENT VERSUS ANGLE OF ATTACK

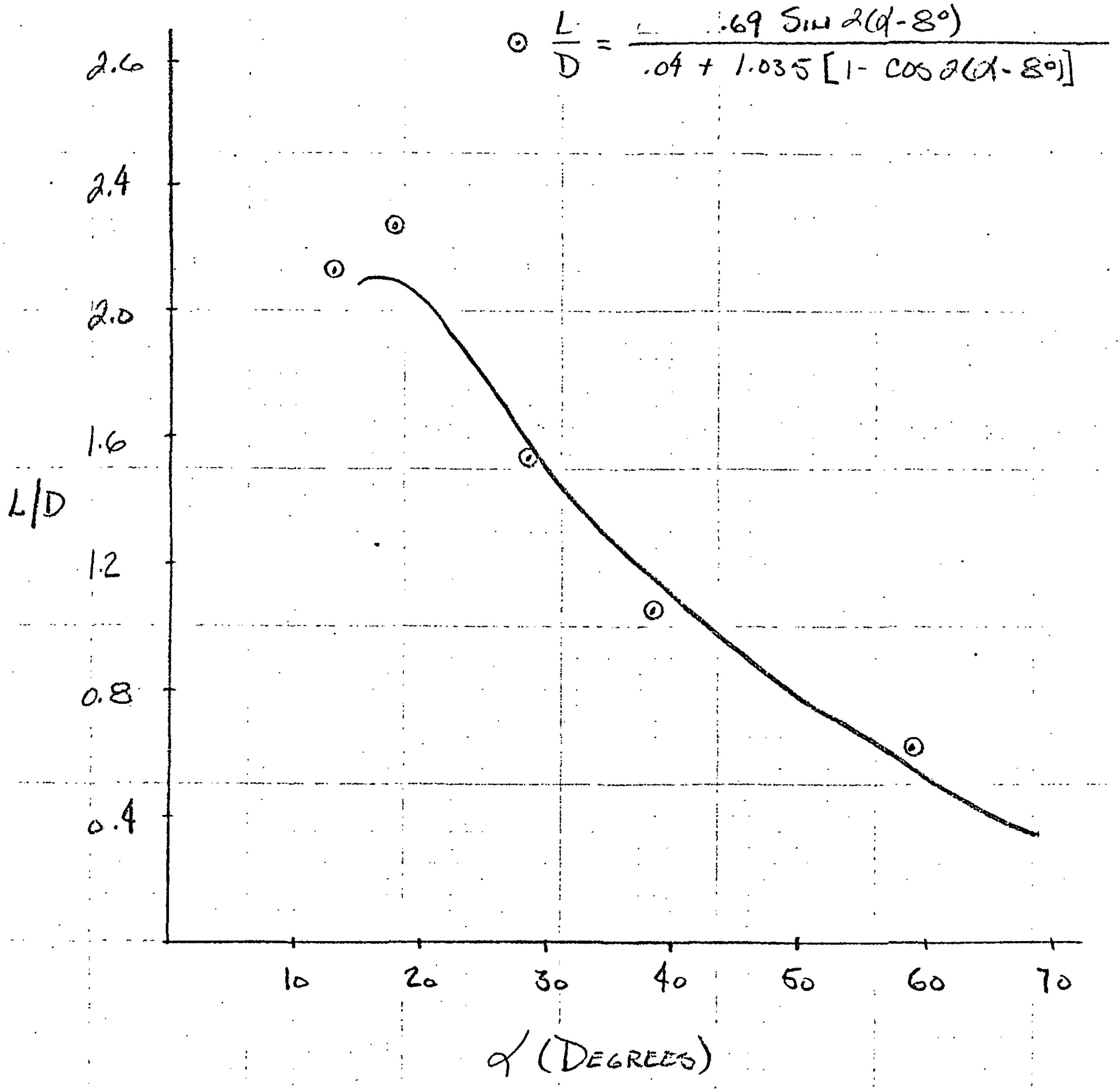

FIGURE A1.1 (c) HYPERSONIC LIFT-TO-DRAG RATIO VERSUS ANGLE OF ATTACK

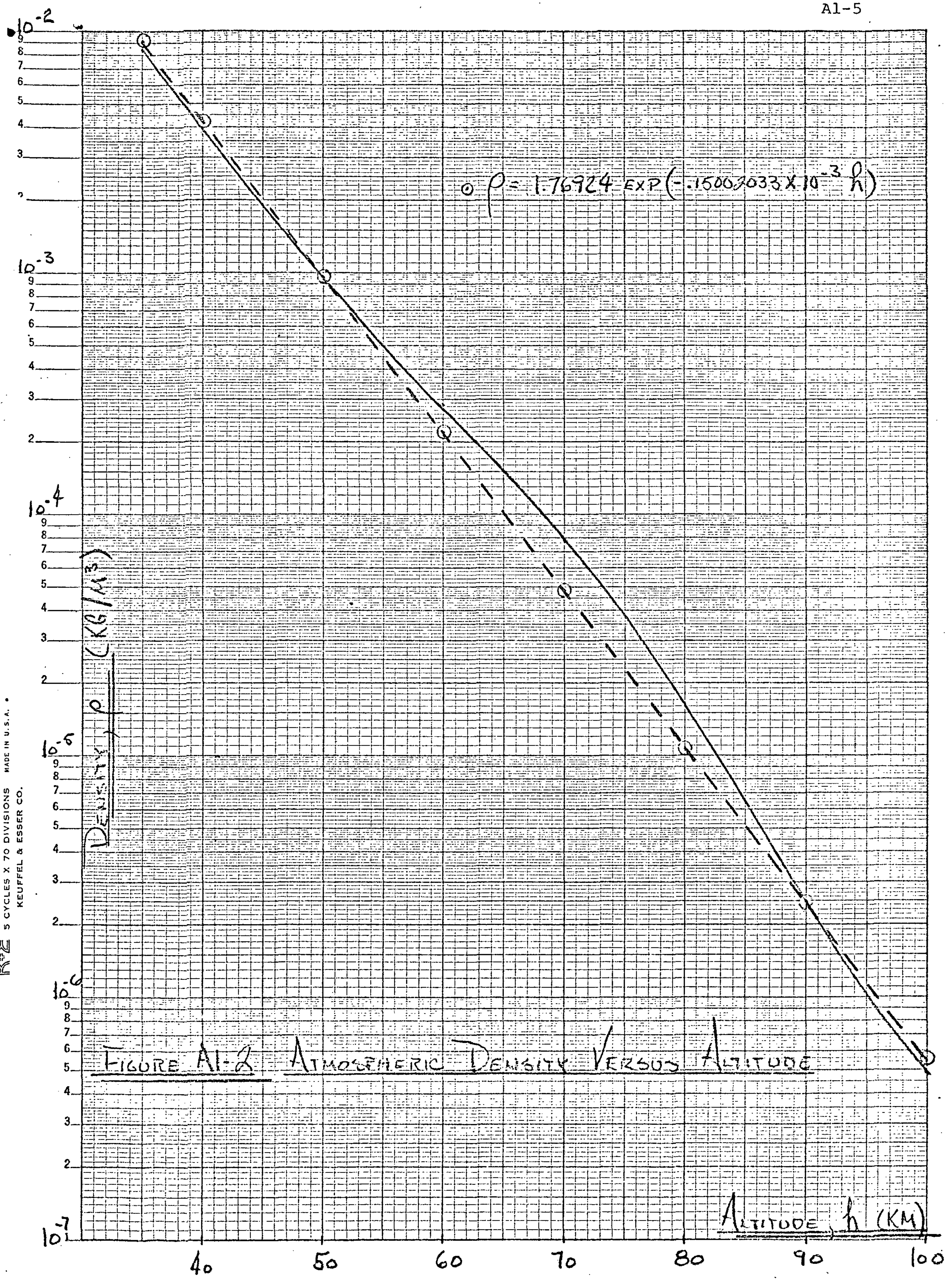

FIGURE A1-2 ATMOSPHERIC DENSITY VERSUS ALTITUDE

Table A1-1 Vehicle and Initial State Data

Vehicle planform area (S) = 836.1 m^2

Vehicle mass (m) = 108864. kg

Initial altitude (h) = 93.0 km

Initial path angle (γ) = -1.1459156°

Initial velocity magnitude (v) = 7.8 km/sec

Initial heading angle (ψ) = 0.0°

Initial cross range (λ) = 0.0°

Initial down range (ϕ) = 0.0°

Vehicle lift coefficient (C_L) = 0.4

Vehicle drag coefficient (C_D) = 0.27

Atmospheric density (ρ) = equation (A1-2) with:

ρ_o = 1.76924 (kg/m^3)

k = 0.15002033 km^{-1}

r_o = 6378.165 km.

A 2 -- Costate Formulation Used to Calculate Reentry Footprint

For the calculation of the reentry footprint, we used a state vector $x^T = (\rho, \phi, \lambda, v, \gamma, \psi)$ and a costate vector $p^T = (p_\rho, p_\phi, p_\lambda, p_v, p_\gamma, p_\psi)$ and maximized the cost functional $J = \theta\lambda_f + (1-\theta)\phi_f$. Since the state differential equations (2-4) and

$$\dot{\rho} = -k\rho v \sin\gamma \qquad (A2\text{-}1)$$

where

$$r = r_o + (\frac{1}{k}) \ln (\rho_o/\rho) \qquad (A2\text{-}2)$$

do not contain ϕ explicitly, p_ϕ is a constant. Hence, in the Mayer formulation we used, the optimal p_ϕ was $(\partial J/\partial\phi_f)$,

$$p_\phi = 1 - \theta \qquad (A2\text{-}3)$$

The control β which maximized the Hamiltonian $H = p^T\dot{x}$ was

$$\begin{aligned} \cos\beta &= p_\gamma \cos\gamma/(p_\gamma^2 \cos^2\gamma + p_\psi^2)^{1/2} \\ \sin\beta &= p_\psi/(p_\gamma^2 \cos^2\gamma + p_\psi^2)^{1/2} \end{aligned} \qquad (A2\text{-}4)$$

We obtained differential equations for costate from $\dot{p}^T = -(\partial H/\partial x)$:

$$\dot{p}_\rho = -vA_u + \frac{(vC_\gamma A_h + 2p_v gS_\gamma + p_\gamma gC_\gamma/v)}{kr\rho}$$

$$\dot{p}_\phi = 0$$

$$\dot{p}_\lambda = \frac{p_\psi v C_\gamma C_\psi}{C_\lambda^2} - \frac{(1-\theta) v C_\gamma C_\psi S_\lambda}{C_\lambda^2}$$

$$\dot{p}_v = -\rho A_u + \frac{p_v D}{mv} + C_\gamma A_h - \frac{2p_\gamma g C_\gamma}{v^2} \qquad \text{(A2-5)}$$

$$\dot{p}_\gamma = -vS_\gamma A_h - \frac{Lp_\psi S_\beta S_\gamma}{mvC_\gamma^2} + p_\rho k_\rho v C_\gamma + p_v g C_\gamma$$

$$\dot{p}_\psi = -\frac{vC_\gamma}{r}\left(p_\lambda C_\psi + \frac{p_\psi S_\psi S_\lambda - (1-\theta) S_\psi}{C_\lambda}\right)$$

Here,

$$A_u = -p_\rho k S_\gamma - \frac{p_v D}{\rho v m} + \frac{L}{m\rho v^2}\left(\frac{p_\psi S_\beta}{C_\gamma} + p_\gamma C_\beta\right)$$

$$A_h = \frac{p_\psi C_\psi S_\lambda}{rC_\lambda} - \frac{p_\lambda S_\psi}{r} + \frac{(1-\theta) C_\psi}{rC_\lambda} + p_\gamma\left(\frac{g}{v^2} - \frac{1}{r}\right)$$

$$g = \mu/r^2$$

and subscripted S and C denote sines and cosines of the subscript angles. Since the Hamiltonian H is not an explicit function of time for this problem, it is a constant of the motion (zero for a free time optimization). Hence, one component of initial costate can be determined so that H = 0. During the actual calculations, we determined $p_v(t_o)$ from the initial values of

p_ρ, p_γ, p_ψ, p_λ, and p_ϕ. State and costate equations were integrated until the desired final altitude was obtained to determine t_f. We chose initial values of p_ρ, p_γ, p_ψ, and p_λ so that final p_γ, p_ψ, p_λ, and p_v were equal to the partial derivatives of J with respect to γ_f, ψ_f, λ_f, and v_f, respectively.

A3 -- Initialization of Costate for Calculating Reentry Footprint

Even when formulated in terms of appropriate spherical coordinates, the region of convergence for optimizing down range and cross range using a linear Newton-Raphson scheme is fairly small. During a preliminary experiment involving a 300-second maximum crossrange trajectory, over 50 trial trajectories were calculated in order to obtain accurate enough initial values for p_ρ, p_γ, p_λ, and p_ψ to converge an optimal trajectory.

In order to avoid calculating extensive trial trajectories for the 93 km. case, the optimal downrange trajectory ($\theta = 0$) was calculated first by holding bank angle β at 0.0 and integrating from $h = 93$ km. to $h = 35$ km. Then final costate components were assigned their optimal values and a back integration was performed to obtain initial costate. We had to use a fairly small (0.35 sec) step size for the fourth order Runge Kutta integration in order to obtain reasonably accurate values of $p(t_o)$. Figure 3-12 illustrates the effect of an inaccurate value for $p(t_o)$ upon p_γ. (When p_γ becomes negative, the reentry vehicle dives sharply, pulling minimum lift).

Once we had obtained an optimal value for $p(t_o)$ for $\theta = 0.0$, we increased θ by 5×10^{-5} twice and iterated to converge these cases. We used converged values of $p(t_o)$ at these three points to initialize a quadratic extrapolation scheme. After each extrapolation of $p(t_o)$ to a new value of θ, we converged $p(t_o)$ and used the new point to continue extrapolating. We were never able to extrapolate through a change in $\Delta\theta$ corresponding to $(\Delta\lambda_f^2 + \Delta\phi_f^2)^{1/2} > 3°$ because of the small region of convergence of the Newton-Raphson iteration.